

Comprehensive Characterization of Solar Eruptions With Remote and *In-Situ* Observations, and Modeling: The Major Solar Events on 4 November 2015

Iver H. Cairns^{*1} · Kamen A. Kozarev² ·
Nariaki V. Nitta³ · Neus Agueda⁴ ·
Markus Battarbee^{5,6} · Eoin P. Carley⁷ ·
Nina Dresing⁸ · Raúl Gómez-Herrero⁹ ·
Karl-Ludwig Klein¹⁰ · David Lario^{11,12} ·
Jens Pomoell¹³ ·
Carolina Salas-Matamoros^{10,14} ·
Astrid M. Veronig¹⁵ · Bo Li¹ ·
Patrick McCauley¹

✉ Iver H. Cairns*
iver.cairns@sydney.edu.au, +61 2 9351 3961

Kamen A. Kozarev
kkozarev@astro.bas.bg

Nariaki V. Nitta
nitta@lmsal.com

Neus Agueda
agueda@fqa.ub.edu

Markus Battarbee
markus.battarbee@gmail.com

Eoin P. Carley
eoincarley@gmail.com

Nina Dresing
dresing@physik.uni-kiel.de

Raúl Gómez-Herrero
raul.gomezh@uah.es

Karl-Ludwig Klein
ludwig.klein@obspm.fr

David Lario
david.larioloyo@nasa.gov

Jens Pomoell
jens.pomoell@helsinki.fi

Carolina Salas-Matamoros
carolina.salas@cinespa.ucr.ac.cr

Astrid M. Veronig
astrid.veronig@uni-graz.at

Bo Li
bo.li@sydney.edu.au

Abstract Solar energetic particles (SEPs) are an important product of solar activity. They are connected to solar active regions and flares, coronal mass ejections (CMEs), EUV waves, shocks, Type II and III radio emissions, and X-ray bursts. These phenomena are major probes of the partition of energy in solar eruptions, as well as for the organization, dynamics, and relaxation of coronal and interplanetary magnetic fields. Many of these phenomena cause terrestrial space weather, posing multiple hazards for humans and their technology from space to the ground. Since particular flares, shocks, CMEs, and EUV waves produce SEP events but others do not, since propagation effects from the low corona to 1 AU appear important for some events but not others, and since Type II and III radio emissions and X-ray bursts are sometimes produced by energetic

Patrick McCauley
mccauley.pi@gmail.com

- ¹ School of Physics, University of Sydney, NSW 2006, Australia
- ² Institute of Astronomy, Bulgarian Academy of Sciences, 1478 Sofia, Bulgaria
- ³ Lockheed Martin Advanced Technology Center, Palo Alto, CA 94304 USA
- ⁴ Dep. Física Quàntica i Astrofísica, Institut de Ciències del Cosmos (ICCUB), Universitat de Barcelona, 08028 Barcelona, Spain
- ¹⁰ LESIA, Observatoire de Paris, PSL Research University, CNRS, Sorbonne Universités, UPMC Univ. Paris 06, Univ. Paris Diderot, Sorbonne Paris Cité, 5 place Jules Janssen, 92195 Meudon, France
- ⁸ Institut fuer Experimentelle und Angewandte Physik, University of Kiel, Germany
- ⁹ Space Research Group, Dpto. de Física y Matemáticas, University of Alcalá, 28871 Alcalá de Henares, Madrid, Spain
- ⁷ Astrophysics Research Group, School of Physics, Trinity College Dublin, Dublin 2, Ireland
- ¹² NASA Goddard Space Flight Center, Heliophysics Science Division, Greenbelt, MD 20771, USA
- ¹¹ formerly at Applied Physics Laboratory, The Johns Hopkins University, Laurel, MD 20723, USA
- ¹³ Department of Physics, University of Helsinki, Helsinki, Finland
- ⁵ Jeremiah Horrocks Institute, University of Central Lancashire, PR1 2HE, UK
- ⁶ University of Turku, Turku, Finland
- ¹⁴ Space Research Center, University of Costa Rica, San José, Costa Rica
- ¹⁵ Kanzelhöhe Observatory & Institute of Physics, University of Graz, 8010 Graz, Austria

particles leaving these acceleration sites, it is necessary to study the whole system with a multi-frequency and multi-instrument perspective that combines both *in-situ* and remote observations with detailed modelling of phenomena. This article demonstrates this comprehensive approach, and shows its necessity, by analysing a trio of unusual and striking solar eruptions, radio and X-ray bursts, and SEP events that occurred on 4 November 2015. These events show both strong similarities and differences from standard events and each other, despite having very similar interplanetary conditions and only two flare sites and CME genesis regions. They are therefore major targets for further in-depth observational studies, and for testing both existing and new theories and models. We present the complete suite of relevant observations, complement them with initial modelling results for the SEPs and interplanetary magnetic connectivity, and develop a plausible scenario for the eruptions. Perhaps controversially, the SEPs appear to be reasonably modelled and evidence points to significant non-Parker magnetic fields. Based on the very limited modelling available we identify the aspects that are and are not understood, and we discuss ideas that may lead to improved understanding of the SEP, radio, and space-weather events.

Keywords: solar energetic particles (SEPs), flares, coronal mass ejections, EUV waves, radio bursts, X-ray bursts, magnetic field, particle propagation

1. Introduction

Solar flares and coronal mass ejections (CMEs) result from magnetic reconnection changing magnetic topologies and releasing energy from magnetic loops and active regions produced by the Sun’s magnetic dynamo. Sufficiently energetic flares and CMEs can produce large-scale propagating waves, most plausibly in the (magnetosonic) fast-mode and Alfvén modes, and pulse-like disturbances. Examples include “EUV waves” observed in the lower corona at EUV wavelengths (Thompson *et al.*, 1998; Warmuth, 2007; Veronig *et al.*, 2010; Patourakos and Vourlidas, 2012; Webb and Howard, 2012), originally called EIT waves (Thompson *et al.*, 1998), and Moreton waves observed in the chromosphere using H_{α} (Moreton, 1960; Uchida, 1968). CMEs and other sufficiently fast plasma motions - not necessarily faster than the fast-mode speed (Pomoell, Vainio, and Kissmann, 2008) - can lead to fast-mode waves that steepen nonlinearly into shocks. Usually idealised as abrupt discontinuities, these shocks compress, heat, and alter the bulk velocity of the plasma, amplify and rotate the magnetic field, and can accelerate particles. CME-driven shocks are visible directly in white-light observations (Vourlidas *et al.*, 2003; Schmidt *et al.*, 2016). Since shocks convert the kinetic energy of a disturbance into thermal, magnetic, and accelerated particle energy, driven shocks are expected to persist longer than blast-wave shocks, for which the shock has propagated well away from the driver.

Originally defined by near-Earth space observations, solar energetic particles (SEPs) are produced between the Sun and Earth as a result of solar activity, as reviewed for example by Reames (1999) and Klecker *et al.* (2006). SEPs have several important space-weather consequences, including radiation damage to

technological systems (*e.g.* degradation of solar cells and electrical circuit components) and humans (*e.g.* astronauts and air travelers), modifying the Earth's radiation belts and environment (Baker *et al.*, 2013), and causing increased particle precipitation into the ionosphere, with associated changes in ionization, plasma density, and radio propagation effects.

The general importance of SEPs and their many associated solar and interplanetary phenomena is that they involve physics that is fundamental, unusually well observed (with high temporal resolution remote imaging data from gamma rays to radio waves, plus *in-situ* particle, magnetic-field, and wave observations), and also widely applicable across the fields of astrophysics, plasma physics, and space physics. For instance, SEP production and propagation involves the acceleration of particles in reconnection regions and by shocks and turbulence, the scattering of particles by magnetic (and electric) field turbulence and self-generated waves, the evolution and dynamics of turbulence, interplanetary magnetic-field connectivity, and the propagation and evolution of CMEs and shocks in the corona and solar wind. Similarly, electrons that are accelerated in solar flares and move down towards the chromosphere lead to (reverse drift) Type III solar radio bursts and X-rays, while the associated downward-going ions produce gamma-rays and X-rays. Precipitation of these particles leads to chromospheric heating, expansion, and evaporation fronts. Electrons accelerated outwards lead to (normal drift) Type III bursts in the corona and solar wind, as well as the prompt component of SEPs; the corresponding ions become prompt SEPs. Shocks, whether blast waves produced by flares or CME-driven shocks, contribute strongly to SEPs; the electrons also produce Type II solar radio bursts in the corona and/or solar wind. Finally, Moreton waves, EUV waves, and EIT waves are signatures of dynamic activity that are sometimes associated with SEP acceleration.

Multiple unresolved issues exist concerning the production and propagation of SEPs from the Sun to Earth, their association with flares, CMEs, and the multiple signatures of activity summarized above, and the physics of these signatures themselves. It is plausible that a definitive answer to the questions of whether and how efficiently coronal shocks accelerate SEPs will require carefully combining in-situ and remote sensing observations with realistic global modelling (*e.g.* Lario *et al.* (2017a)). These observations and models will not only be for SEPs but also for the related phenomena of flares, erupting filaments and CMEs, EUV and Moreton waves, and Type II and III bursts. Some of these, especially the propagation and properties of CMEs and their white-light/EUV and Type II radio signatures, are also relevant to forecasting space weather (Schmidt, Cairns, and Hillan, 2013; Cairns and Schmidt, 2015; Kozarev *et al.*, 2015; Schmidt and Cairns, 2016b,a). Resolving these issues is a major focus of the *Parker Solar Probe* (Fox *et al.*, 2016) and *Solar Orbiter* (Müller *et al.*, 2013) missions.

In this article we briefly review and summarise these issues and then address them using the major solar and interplanetary events associated with the events of 4 November 2015. Arguably these are an ideal set of events to study. First, all three are major events that occur in essentially the same coronal and interplanetary configurations (*e.g.* the same large-scale magnetic connectivity and structures such as streamers and coronal holes) and conditions (except for

seed energetic particles) but with two sites for the flares and associated CMEs. Both these are on the side of the Sun facing Earth, one near the west limb and one near disk center. Second, a very complete set of ground-based and spacecraft observations exists, ranging from remote X-ray to radio wavelengths for light to *in-situ* plasma, field, and energetic particle measurements, making these events amenable to comprehensive data-theory comparisons. Third, significant SEP, space-weather, flare, CME, EUV wave, Moreton wave, hard X-ray, microwave, and radio events were produced, all of direct interest for observers, theorists, modelers, simulators, and operational space-weather staff. What is more, a relatively complete set of observations exists for these. Fourth, the events show strong commonalities (M-class flares, observable EUV waves, CMEs, and Type II and III bursts), yet also strong differences (magnetic connectivity, SEP occurrence, and radio bursts. Fifth, an unusually strong space-weather event occurred in association with the third event on 4 November 2015, especially with regard to aviation radar systems (Marqué *et al.*, 2018).

Our primary goal is to detail the solar and interplanetary observations for the three events, describing the common and different features, identifying the aspects that are and are not understood now, and providing the basic observations in a form amenable for future, more detailed, comparisons with theoretical and modeling analyses. The secondary goal is to make progress on understanding these solar and interplanetary phenomena, especially those associated with SEPs, shocks, and magnetic-field configurations, by showcasing the necessary elements of a comprehensive analysis including multi-instrument observations and relevant modeling.

The article proceeds by reviewing the issues involved with SEPs, flares, shocks, CMEs, waves, and related signatures (Section 2). It then describes the evolution of the parent active regions, coronal magnetic field, and the X-ray and microwave flares for the 4 November 2015 events (Section 3). The failed filament eruptions for the first two flares, the Moreton wave for the first flare, and the EUV waves and CMEs for all three flares are described in Section 4 and shown to be mutually consistent. Section 5 overviews the radio events, including the properties of the over five Type IIs involved, the relative lack of Type IIIs, and the strong microwave and Type IV emission for the first and third events. Section 6 details the interplanetary plasma and magnetic field context, showing the arrival of a shock early on 4 November associated with an earlier event and the shock and CME associated with the third event. The SEP observations are detailed in Section 7. The space-weather aspects of the events are briefly discussed in Section 8. A summary of the observations and associated theoretical implications is provided in Section 9.

2. Detailed Theoretical and Observational Context

SEPs consist of electron, proton, and ion populations with energies in the range of tens of KeV to a few GeV. SEP events can be loosely categorized into impulsive and gradual events, distinguished by the timescales of their intensity profiles and properties such as composition and ionization states (Luhn *et al.*, 1984;

Cane, McGuire, and von Rosenvinge, 1986; Reames and Stone, 1986; Reames, 1988; Luhn *et al.*, 1987; Reames, 1999; Klecker *et al.*, 2006). Impulsive events are attributed to particle acceleration in regions producing solar flares, presumably in magnetic-reconnection regions, and gradual events to acceleration by CME-driven shocks. However, a number of events exhibit characteristics of both impulsive and gradual events (*i.e.* timing of intensity profiles and ratios of heavy ions at high energies with hybrid characteristics), blurring the distinction between acceleration at reconnection sites and at shocks (Kallenrode, Cliver, and Wibberenz, 1992; Torsti *et al.*, 2002; Klecker, Möbius, and Popecki, 2006).

In-situ observations of CME-driven shocks and their associated energetic particles have shown that particle acceleration at shocks typically results from shock drift acceleration in the quasi-perpendicular regime and diffusive shock acceleration in the quasi-parallel regime (*e.g.* Lee, 1983; Decker and Vlahos, 1986; Kennel *et al.*, 1986; Jones and Ellison, 1991; Lee, 2005; Cohen, 2006; Desai and Giacalone, 2016, and references therein). Here the two regimes are defined in terms of θ_{Bn} , the angle between the upstream magnetic field \mathbf{B} and the normal to the local shock surface: the quasi-perpendicular and quasi-parallel regimes correspond to $45^\circ \lesssim \theta_{Bn} \lesssim 90^\circ$ and $\theta_{Bn} \lesssim 45^\circ$, respectively. Without *in-situ* measurements of shocks and magnetic fields in the corona, determining which acceleration processes take place close to the Sun is very challenging and requires careful examination of multi-wavelength remote observations.

Analyses of white light and EUV observations, supported by radio imaging and radio Type II dynamic spectra, have found that shocks can form as low in the corona as heliocentric distances of 1.2 to 2.2 R_\odot (Klassen *et al.*, 1999; Veronig *et al.*, 2010; Ma *et al.*, 2011; Bain *et al.*, 2012; Gopalswamy *et al.*, 2013; Carley *et al.*, 2013; Nitta *et al.*, 2014), where R_\odot denotes the solar radius. Several mechanisms can give rise to shock formation in the corona, including blast waves caused by a sudden release of flare-related energy (Vršnak *et al.*, 2006) and erupting CMEs which drive shocks as they propagate outwards (Dauphin, Vilmer, and Krucker, 2006; Zimovets *et al.*, 2012). Determining whether blast-wave or CME-driven shocks are relevant to particular events (Howard and Pizzo, 2016), and especially to associated Type II bursts and EUV waves, is of particular interest (Cane and Erickson, 2005; Cairns, 2011). Essentially all interplanetary Type II bursts are interpreted in terms of CME-driven shocks (Reiner *et al.*, 1998; Bale *et al.*, 1999; Cairns, 2011), but this may not be correct for coronal Type IIs.

Type II bursts are interpreted theoretically in terms of: shock-drift acceleration and magnetic mirror reflection of electrons at shocks; development of a beam distribution of reflected electrons; growth of Langmuir waves via the beam instability; and nonlinear wave-wave processes that convert Langmuir wave energy into radio emission near the electron plasma frequency f_{pe} and near $2f_{pe}$ (the so-called fundamental and harmonic radiation, respectively). Relevant reviews include those of Nelson and Melrose (1985), Bastian, Benz, and Gary (1998), and Cairns (2011). These theories require the source regions to be where the shock is strongly quasi-perpendicular with $80^\circ \lesssim \theta_{Bn} \lesssim 90^\circ$ (Holman and Pesses, 1983; Cairns, 1986; Knock *et al.*, 2001; Schmidt and Cairns, 2012; Cairns and Schmidt, 2015; Schmidt and Cairns, 2016a). Interestingly, multi-frequency

mapping of some Type II bursts shows that source regions at different frequencies can be aligned along a direction that is strongly inclined to the radial (Nelson and Robinson, 1975; Klein *et al.*, 1999). This is not expected if the electrons are produced at quasi-perpendicular regions of the shock (*e.g.* near the nose for overlying loop fields or at lateral expanding flank regions for quasi-radial fields) or at quasi-parallel regions of the shock (*e.g.* near the nose for quasi-radial \mathbf{B}). Recent semi-empirical studies (Kozarev *et al.*, 2015; Lario *et al.*, 2017a) have suggested that the regions of expected shock acceleration may vary with time, and may move to different locations on the shock surface, depending on the parameters governing acceleration efficiency. Combining remote observations with modeling approaches allows determination of relevant parameters for electron and ion acceleration: θ_{Bn} , the spatial profile of the Alfvén speed V_A , and the lateral expansion of the driving CME (Warmuth and Mann, 2005; Temmer, Vrsnak, and Veronig, 2013; Zucca *et al.*, 2014; Kozarev *et al.*, 2015; Lario *et al.*, 2017a,b).

Recent high-cadence observations of large-scale coronal transients, known as “EUV waves” (or “EIT waves”, “coronal bright fronts (CBFs)”, and “large-scale coronal propagating fronts (LCPFs)”), suggest that they are signatures of magnetosonic waves or shocks (Warmuth *et al.*, 2004; Veronig *et al.*, 2010; Kozarev *et al.*, 2011; Downs *et al.*, 2012). Here we consistently use the term “EUV waves” to avoid unnecessary confusion. EUV waves have been widely studied in the last several years due largely to the significantly improved EUV images in terms of spatial and temporal resolution, spectral coverage, and multipoint views available from the *Solar and Heliospheric Observatory* (SOHO), *Solar and TERrestrial RELations Observatory* (STEREO), and *Solar Dynamics Observatory* (SDO). We now know that EUV waves are very common during sufficiently impulsive solar eruptions and several studies have characterized them in detail (Veronig *et al.*, 2010; Patsourakos, Vourlidas, and Stenborg, 2010; Hoilijoki *et al.*, 2013).

The ubiquity of EUV waves during solar eruptions has raised the question of whether they signify shocks or compression waves responsible for accelerating particles observed during the early stages of SEP events. Extending classic works (Krucker *et al.*, 1999; Torsti *et al.*, 1999), recent analysis of the temporal relation between the evolution of EUV waves on the solar disk and the *in-situ* onset of SEP fluxes for a large sample of events during Cycle 23 has shown a general consistency with wave/shock acceleration for protons but not for electrons (Miteva *et al.*, 2014a). Correspondingly, some analyses find evidence for SEP injections when EUV waves reach the magnetic footpoint of the spacecraft (Rouillard *et al.*, 2012) whereas others do not (Miteva *et al.*, 2014b; Lario *et al.*, 2014). This discrepancy points to the likely complexity of the interactions between the EUV wave, shock (whether blast-wave or CME-driven), CME, flare, and the global coronal magnetic field.

The two STEREO spacecraft and the near-Earth spacecraft *Advanced Composition Explorer* (ACE), SOHO, and *Wind* allow study of SEP events from multiple vantage points. Observing the same event from a broad range of longitudes (Dresing *et al.*, 2012; Lario *et al.*, 2013; Dresing *et al.*, 2014; Lario *et al.*, 2014; Gómez-Herrero *et al.*, 2015, *e.g.*) allows us to constrain the longitudinal

extent of particle acceleration by shocks and associated magnetic connectivity. For some events very different SEP fluxes and profiles are observed at closely separated spacecraft (Klassen *et al.*, 2016), for others the entire SEP event is very localised in longitude, and for still others the SEP event is observed at all longitudes. These observations and complementary modeling efforts are beginning to unravel the complexity in time, longitude, energy, and species of particle acceleration and transport through the inhomogeneous coronal and solar wind (Pacheco *et al.*, 2017; Afanasiev and Vainio, 2013; Kozarev *et al.*, 2013), as well as the associations with radio emissions (Cane, Erickson, and Prestage, 2002; Schmidt, Cairns, and Lobzin, 2014; Cairns and Schmidt, 2015; Schmidt and Cairns, 2016a).

The properties of the seed-particle distributions incident on the shock (whether from the ambient background, a flare site, or pre-processed by another event) also affect both the shock-accelerated particle distribution functions (*e.g.* the “injected” particles subject to propagation analyses (Battarbee *et al.*, 2013; Agueda *et al.*, 2014)) and related phenomena such as Type II bursts (Cairns *et al.*, 2003; Knock *et al.*, 2003; Kozarev *et al.*, 2015; Schmidt *et al.*, 2016; Lario *et al.*, 2017b). The properties of pre-existing and self-generated turbulence also affect the effectiveness of diffusive shock acceleration (*e.g.* Vainio *et al.* (2014)). Similarly, in-situ observations of relativistic electrons and ions yield injection / release times and propagation distances that constrain the locations and duration of acceleration events and the effectiveness of wave-particle scattering and diffusion between the source and observer, *e.g.* Agueda *et al.* (2014).

Magnetic connectivity between the SEP source and the observing location is required, unless sufficient cross-field scattering and diffusion exist, for SEPs to be observed. This requires particles to either be accelerated on field lines connecting to the observer or have access to these open field lines (Lario *et al.*, 2017b). Modeling of solar and interplanetary magnetic structures is then required, for instance using PFSS or other approaches such as MHD simulations (Luhmann *et al.*, 2017), the Archimedean (hereafter Parker) spiral (Parker, 1958), or generalized data-driven models (Li *et al.*, 2016).

We return to diagnostics of particle acceleration in flares, clearly vital if the effects of shocks and flares are to be identified, separated, and constrained in detail. Flare signatures are observed at H_α , white-light, UV to EUV, X-ray, and gamma-ray wavelengths. Flares involve substantial heating (sometimes to over 10 MK (Lin *et al.*, 1981; Caspi, Krucker, and Lin, 2014)), changed magnetic topologies, and particle acceleration. Magnetic reconnection is thus directly relevant but other processes likely contribute to the heating and particle acceleration (Fletcher *et al.*, 2011). The spatial sizes of flaring regions vary widely, from very compact regions (*e.g.* the size of low-lying loops) to the size of entire active regions. Similarly the corresponding time-scales and total energy releases also vary widely, from impulsive to long duration and classes A to X, respectively.

Thermal emission from the heated plasma is one component of flare radiation (*e.g.* soft X-rays and UV and EUV radiation). Radiation is also emitted by or as a result of energetic particles precipitating into the chromosphere from higher-up acceleration regions; examples include H_α radiation and EUV radiation, as well as X-rays produced by bremsstrahlung from energetic electrons with either

thermal or nonthermal distribution functions. The X-ray spectra and timescales of bursts can distinguish between thermal and non-thermal electron populations (Holman *et al.*, 2011).

Another crucial signature of electron acceleration, but also of connection to open magnetic field lines, are Type III solar radio bursts (Suzuki and Dulk, 1985; Bastian, Benz, and Gary, 1998; Li, Cairns, and Robinson, 2008; Reid and Ratcliffe, 2014). These involve the accelerated electrons developing a beam distribution function by time-of-flight effects, growth of Langmuir waves by the beam instability, and nonlinear coupling of the Langmuir waves to produce f_p and $2f_p$ radiation. Type IIIs thus are believed to differ from Type IIs in the source of the accelerated electrons, the beam's detailed formation mechanism, and the beam's characteristic speed (speeds greater than 20 electron thermal speeds it versus 3). Type IIIs have widely different starting and ending frequencies, intensities, and drift rates and can drift to lower and higher frequencies, corresponding conventionally to electrons moving away from (normal frequency drift) and towards (reverse frequency drift) the Sun, respectively. The specific reasons Type IIIs are important for SEP, flare, and CME physics is that they are signatures of open magnetic fields accessible to accelerated electrons, are interpreted in terms of electron acceleration in magnetic reconnection regions, and can lead to SEP particles.

Velocity dispersion analyses of the energetic electrons in Type III and SEP events yield injection times and estimated propagation distances (presumably along \mathbf{B} and assuming negligible energy losses) (Lin, 1985). The time-varying pitch-angle distributions can also be compared with theoretical predictions and used to constrain the timing, number, and relative sizes of injections of energetic particles and the transport conditions along the observer's magnetic field line(s) (Agueda *et al.*, 2014). These constraints can then be compared with independent arguments based on the timing, spatial locations, and magnetic connectivity of Type II and III bursts, flares, CMEs, and shocks. A major issue with understanding SEP electrons associated with Type IIIs is that the relativistic electrons appear to have injection times that are typically 10–20 minutes later than the sub-relativistic electrons (energies $\approx 10 - 50$ KeV) that produce Type III bursts near 1 AU (Krucker *et al.*, 1999; Haggerty and Roelof, 2002; Haggerty, Roelof, and Simnett, 2003).

Numerical simulations and associated theoretical formalisms for predicting the acceleration and transport of ion SEPs typically involve idealisations concerning one or more of the mean free path, scattering, magnetic field, dimensions, shock geometry, acceleration process, or imposed analytic approximations. For instance, the wave-particle scattering near the shock may be calculated with full time-dependent self-consistency (Ng, Reames, and Tylka, 2003) or assumed to proceed to completion with a steady-state diffusive shock acceleration solution (Lee, 1983, 2005; Zank, Rice, and Wu, 2000; Li, Zank, and Rice, 2005; Li *et al.*, 2009; Verkhoglyadova *et al.*, 2010; Vainio *et al.*, 2014; Hu *et al.*, 2017). Similarly a constant mean free path may be assumed for the particle transport (Marsh *et al.*, 2013, 2015) or magnetic moment-induced focusing to small pitch-angles, magnetic-turbulence effects, and associated pitch-angle scattering included (Jokipii, 1966; Matthaeus *et al.*, 2003; Zhang, Qin, and Rassoul, 2009;

Shalchi, Li, and Zank, 2010; Hu *et al.*, 2017), or cross-field diffusion (Zhang, Qin, and Rassoul, 2009; Dröge *et al.*, 2014; He and Wan, 2015). Typically, the background magnetic field is assumed to be Parker-like and drift effects are ignored, but drift effects are sometimes included and found important (Marsh *et al.*, 2013, 2015) and the magnetic field is sometimes significantly non-Parker-like (Schulte in den Bäumen, Cairns, and Robinson, 2011, 2012; Li *et al.*, 2016). Finally, the formalisms available sometimes go beyond the usual one-dimensional approximation to two dimensions (Kozarev *et al.*, 2013), or even three (Zhang, Qin, and Rassoul, 2009; Marsh *et al.*, 2013, 2015), and they can couple simulations of specific CMEs and their shocks with the particle transport formalism (Zank, Rice, and Wu, 2000; Verkhoglyadova *et al.*, 2010; Kozarev *et al.*, 2013; Hu *et al.*, 2017). Existing theory and simulations thus often experience major challenges explaining observed SEP events.

3. Active Region Evolution, X-ray, Microwave, and Optical Flares

We begin the analysis of the 4 November 2015 solar eruptions with an overview of the source active regions, followed by the X-ray and microwave flare observations that define the initial stages of the three events. Table 1 provides a summary of these and other associated observations.

3.1. Source Active Regions

Figure 1 overviews the Sun on 4 November 2015, showing a full-disk continuum image and a line-of-sight magnetogram from the *Helioseismic and Magnetic Imager* (HMI; Scherrer *et al.*, 2012) onboard SDO together with an H_{α} filtergram from the Kanzelhöhe Observatory (Pötzi *et al.*, 2015). The two most prominent active regions present on the visible solar hemisphere on 4 November are NOAA AR 12443 located close to disk center (N6,W10), which is the source of Event 3, and AR 12445 located close to the western limb (N16,W76), which is the source of Events 1 and 2. AR12445 emerged and evolved very fast, over a period of four days, whereas AR 12443 was a long-lived active region.

NOAA AR 12443 is an extended AR region of McIntosh class Fck and magnetic Hale class $\beta\delta$ on 4 November. It developed when it was on the back side of the Sun and rotated onto the visible solar hemisphere on 28 October 2015. Figure 2 shows snapshots of the evolution of NOAA AR 12443 on four days before 4 November when it produced Event 3 of our study. In contrast, AR 12445 developed very quickly. Figure 3 shows the evolution of NOAA AR 12445 from 1 November when it was first visible and its fast flux emergence and development until 4 November, when it produced Events 1 and 2. On 4 November, its McIntosh class was Ekc and Hale class $\beta\delta$.

3.2. X-ray and Microwave Emission for the Three Flares on 4 November 2015 – Flare-related Electron Acceleration and Escape

The microwave, soft, and hard X-ray emissions (SXR and HXR, respectively), associated with the three flares on 4 November 2015, are signatures and indicators of the electron-heating and acceleration processes occurring in the flaring active regions. HXRs at photon energies above about 20 KeV are dominantly bremsstrahlung from nonthermal electrons interacting with the dense low corona and chromosphere. Microwaves, that is radio emission at frequencies between 1 GHz and several tens of GHz, are usually attributed to gyrosynchrotron radiation of electrons with energies between about 100 KeV and a few MeV. It is necessary to look at the behavior of the spectrum in order to identify potentially competing processes: weak (flux densities below 100 sfu), slowly evolving bursts can also be due to thermal bremsstrahlung, and emission up to a few GHz to collective plasma processes.

3.2.1. Event 1

Event 1 occurred at heliographic position (N15,W64) and reached GOES class M1.9 (GOES start time: 03:20 UT, peak time: 03:26 UT). The time histories of the RHESSI *Hard X-Ray* (HXR), GOES *Soft X-Ray* (SXR) and the microwave emission from the *Nobeyama Radio Polarimeters* (NoRP) of the first flare are displayed in Figure 4. They show an impulsive HXR and microwave burst during the rise phase of the SXR burst. The RHESSI HXR burst is observed to high energies, up to about 500 KeV, with the peaks near 03:24 UT above 25 KeV and the 3 – 12 KeV channels peaking near 03:25 UT. The microwave flux density spectrum has its maximum between 17 and 35 GHz, with a peak flux density of about 950 sfu near 03:24 – 03:25 UT. Although not exceptionally high, the flux density is well above values that can be achieved by thermal bremsstrahlung. The burst is hence due to gyrosynchrotron emission. The combination of a high peak frequency and moderately high flux density suggests that the emission occurs in a compact source with rather strong magnetic field, presumably at low coronal altitudes. The strong HXR and microwave emissions show that the parent flare is a very efficient accelerator of electrons to near-relativistic energies.

Figure 5 shows snapshots of Event 1 observed by the SDO / Atmospheric Imaging Assembly (AIA) using the 131 Å EUV filter, sensitive to hot flaring plasma at temperatures of about 10 MK. The three images shown are recorded during the early rise, the peak and decay phase of the event. We overplot RHESSI 6 – 12 and 30 – 100 KeV sources as well as a 17 GHz microwave image synthesized during the peak of the event from the Nobeyama Radioheliograph (NoRH). The RHESSI images have been reconstructed with detectors 2 to 8 (Lin *et al.*, 2002; Hurford *et al.*, 2002), but even with the fine grids included we are not able to resolve the emission from the flare loop and footpoints. All three instruments show that the flare is very compact, with the flare emission originating from a small loop arcade. The endpoints of the loops coincide with flare kernels observed in AIA 1700 Å. From the RHESSI and AIA images we

estimate the distance between the loop footpoints to be about 20 Mm, and the loop height < 10 Mm. These characteristics support the interpretation of the high peak microwave frequency observed by NoRP being due to the microwaves originating at low coronal altitudes in a compact source. The AIA 131 Å sequence plotted in Figure 5 also shows the impulsive filament eruption towards the South that also originates from the flaring region.

Table 1. Short summary of the phenomena associated with the events of 4 November 2015.

Event #	AR Location	SXR start time [UT]	GOES X-ray class	HXR	GHz	Type IIs	Type IIIs	EUV wave speed [km s ⁻¹]	CME speed [km s ⁻¹]	Shock / CME at Earth	Space weather	SEPs
1	12445 N15W64	03:20	M1.9	impulsive	Yes No IP	Metric IP	Weak metric	750 S-SE dir.	328 PA 280°	No / No	No	Electrons No ions
2	12445 N12W73	11:55	M2.6	short & weak	No No IP	Metric No IP	No metric	600 S-SE dir.	252 PA 280°	No / No	No	No electrons No ions
3	12443 N09W04	13:31	M3.7	strong & hard	Yes IP	Metric IP	Metric	700 N-NW dir.	580 Halo	Yes / Yes	Yes	Electrons Ions

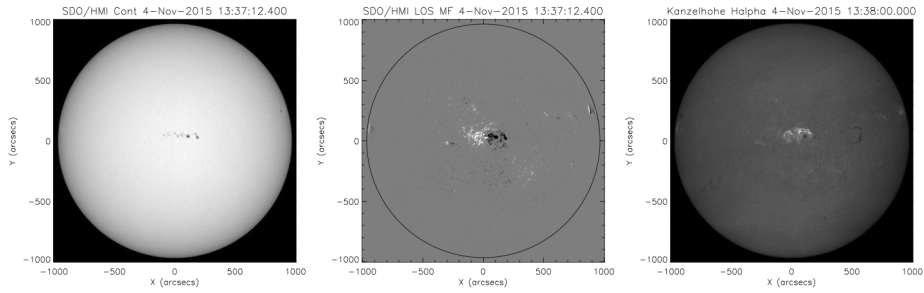


Figure 1. Overview of the Sun at 13:37 UT on 4 November 2015. (*Left*) SDO/HMI continuum image, (*middle*) SDO/HMI line-of-sight magnetogram, (*right*) H_{α} image from the Kanzelhöhe Observatory, all recorded during the rise phase of Event 3.

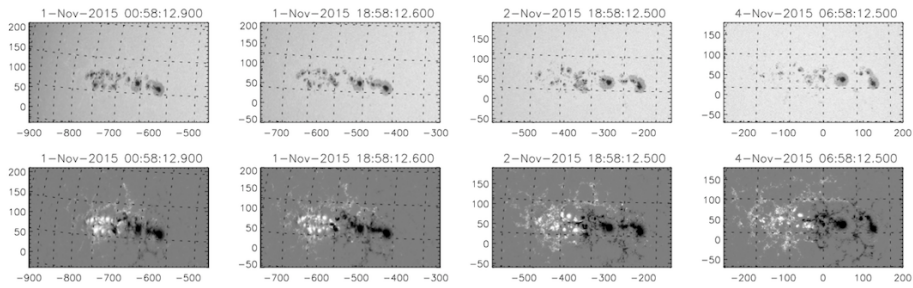


Figure 2. Evolution of NOAA AR 12443 from 1 to 4 November 2015. (*Top*) SDO/HMI continuum images and (*bottom*) SDO/HMI line-of-sight magnetograms (with the grayscale saturated at ± 1000 G).

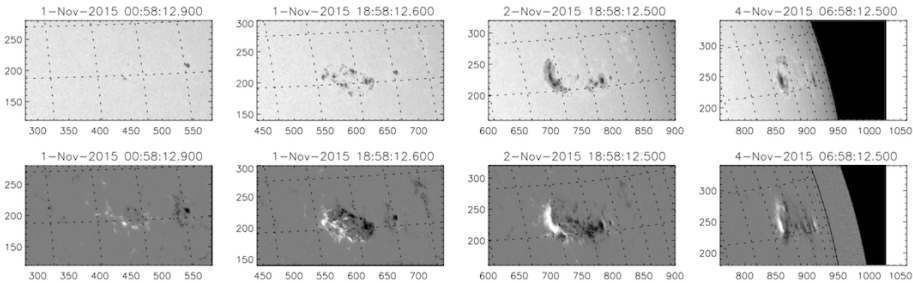


Figure 3. Evolution of NOAA AR 12445 from 1 to 4 November 2015. (*Top*) SDO/HMI continuum images and (*bottom*) SDO/HMI line-of-sight magnetograms (with the grayscale saturated at ± 1000 G).

3.2.2. Event 2

The RHESSI HXR time profiles of the two later events are shown in Figure 6. Event 2 occurred at heliographic position N12W73 and reached GOES class

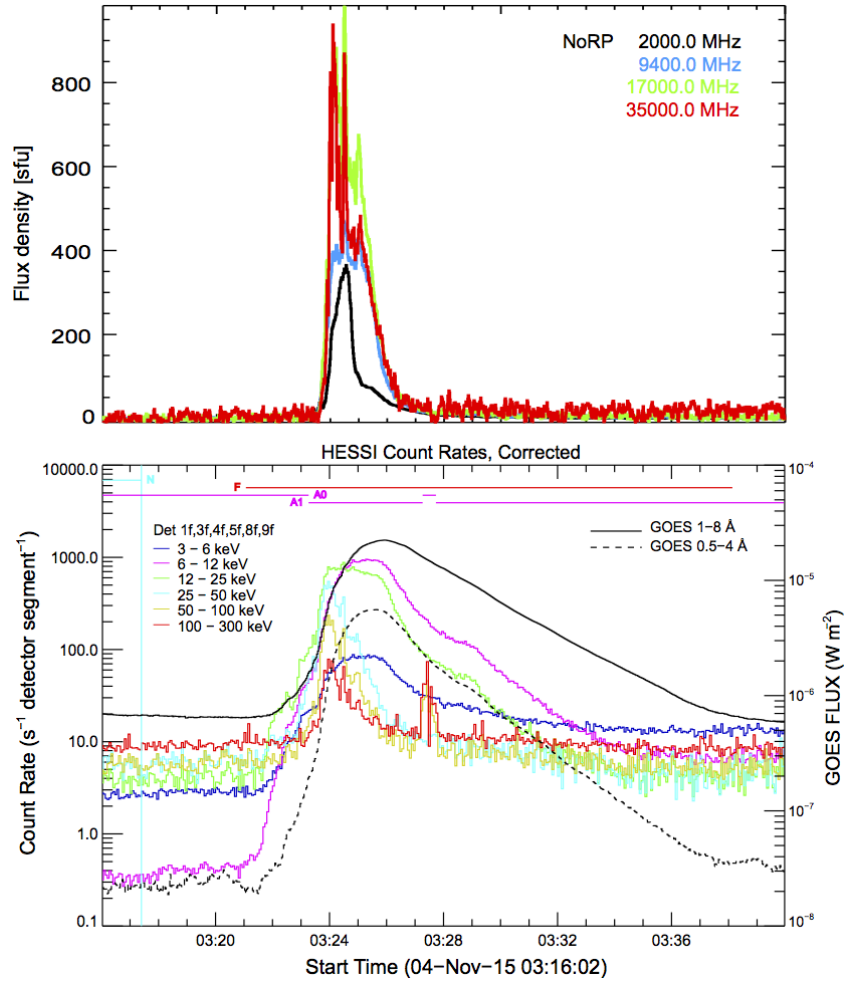


Figure 4. Temporal histories of the NoRP microwave (*top panel*), RHESSI HXR, and GOES SXR (*bottom panel*) emission during Event 1.

M2.6 at (GOES start time: 11:55 UT, peak time: 12:03 UT). RHESSI covered the full impulsive phase of Event 2 and observed enhanced HXR emission up to energies of about 50 KeV. The HXR emission of this event is clearly weaker and softer than the first event. However, the AIA 131 Å and RHESSI images plotted in Figure 7 reveal that Event 2 is homologous with Event 1, as regards the occurrence in the same region, the small and compact flare loops (also reflected in the short HXR and SXR emission profiles), and the associated ejection of filament material toward the south. At microwave frequencies RSTN (*Radio Solar Telescope Network*, operated by the US Air Force) sees a weak burst of gyrosynchrotron emission with peak frequency 8.8 GHz, between 12:00 and 12:04 UT. Despite the homology, Event 2 is a much less efficient electron accelerator than Event 1 based on the X-ray and microwave emissions.

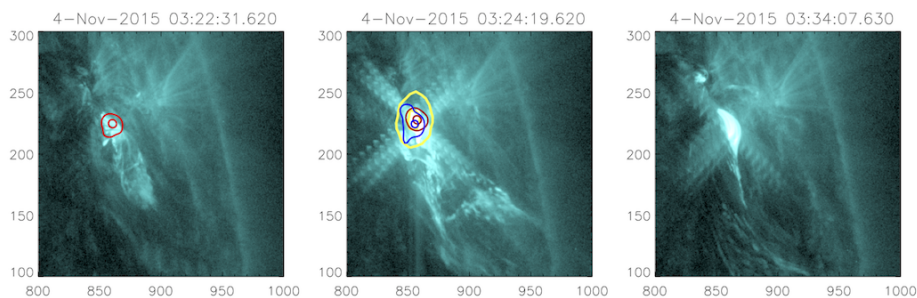


Figure 5. Snapshots showing the evolution of Event 1 in AIA 131 Å filtergrams. Red and blue lines are contours from RHESSI X-ray images reconstructed during the early rise phase (*left*) and peak (*middle*) in the 6 – 12 and 30 – 100 KeV energy bands, respectively. The *rightmost image* is after the event. Yellow contours are from a NoRH 17 GHz image at event peak. Units are arcseconds from Sun center.

3.2.3. Event 3

Event 3 occurred close to disk center, at heliographic position (N09,W04). It is the largest of the three events under study, with a GOES class M3.7 (start time: 13:31 UT, peak time: 13:52 UT). GOES and RHESSI light curves are shown in the bottom panel of Figure 6. Classifying the GOES light curves in Figures 4 and 6 using the system of Cane, McGuire, and von Roseninge (1986), Events 1 and 2 are impulsive events and Event 3 a gradual event. The RHESSI hard X-ray observations are restricted to before 13:43 UT due to spacecraft night. However, a comparison with the light curves from *FERMI*/GBM shows that RHESSI missed no major burst. The HXR burst is observed up to photon energies of about 100 KeV. The radio emission, however, does show efficient electron acceleration, starting with a moderately strong burst with peak frequency near 9 GHz in the impulsive phase (\approx 13:38–13:50), and followed by a long-duration burst in the post-impulsive phase (14:00–15:00 UT; Type IV burst) that was mainly observed at frequencies below 3 GHz (cf. Section 5). Figure 8 shows snapshots during the early rise, peak, and decay phase of Event 3 in AIA 131 Å together with RHESSI HXRs. In contrast to the compact Events 1 and 2, Event 3 shows an extended flare arcade. The East-West extent of the overall flaring region as observed in the AIA EUV emission is about 140 Mm. The RHESSI emission is concentrated mostly to the brightest flaring loops observed in AIA 131 Å (compare the middle and right panels), with a loop footpoint separation of about 50 Mm, corresponding to a loop apex height of 25 Mm for a semicircular loop.

4. Failed Filament Eruptions, EUV Waves, and CMEs

4.1. Filament Eruptions and EUV Waves

Figure 9 summarises the eruption evolution seen in EUV for the three events, clearly showing moving material and propagating wave features in all three cases. Red, green, and blue colors correspond to AIA data number values for the filters

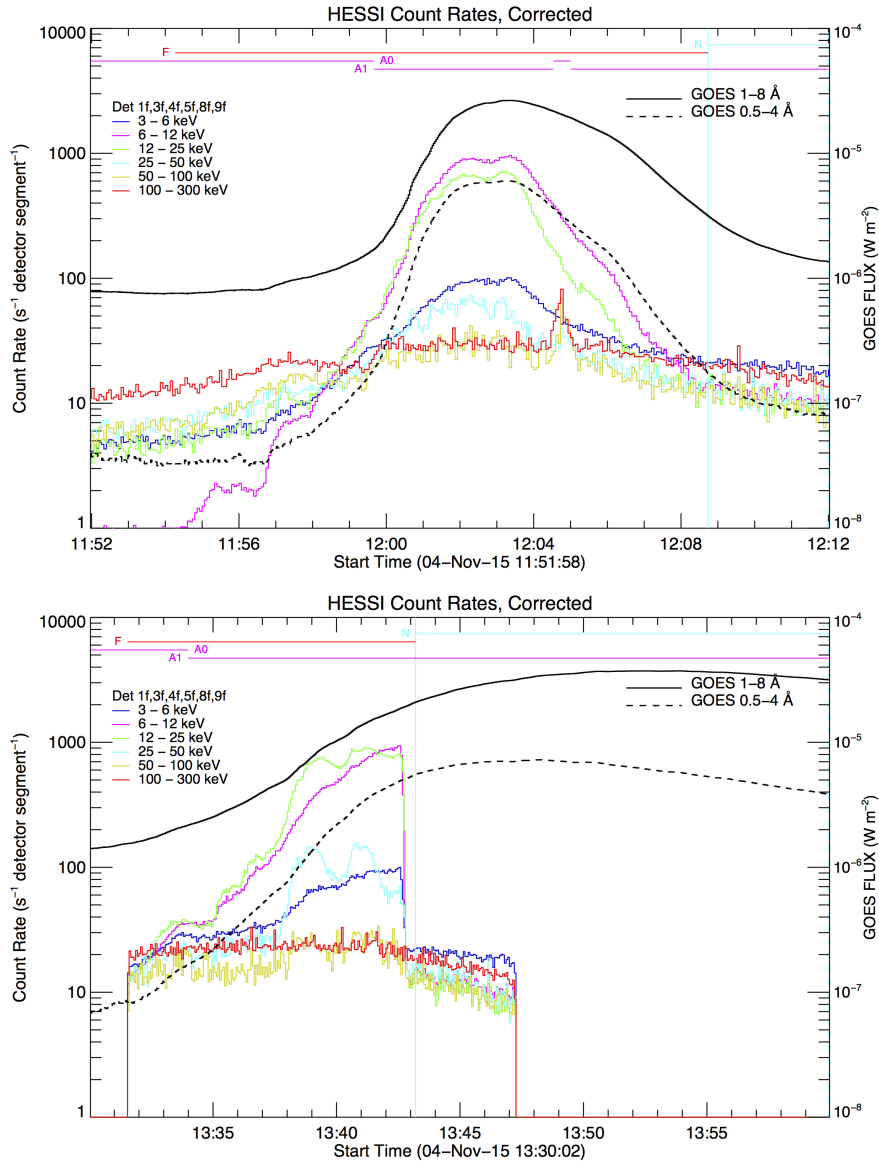


Figure 6. Time histories of the RHessi HXR emission during Event 2 (*top*) and Event 3 (*bottom*).

171, 193, and 211 Å, respectively. Events 1 and 2 show very similar morphology eruptions off the west limb, generally directed towards the south, while Event 3 shows the event at disk center, beginning with a brightening of coronal loops, followed by the propagation of a diffuse front, largely in northwesterly direction out to $\approx 50^\circ$ W longitude, before decreasing in intensity.

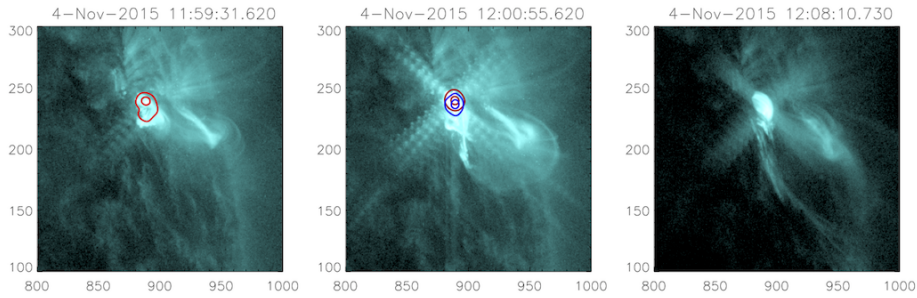


Figure 7. Snapshots showing the evolution of Event 2 in AIA 131 Å filtergrams. Red and blue lines are contours from RHESSI X-ray images reconstructed during the early rise phase (*left*) and peak (*middle*) in the 6 – 12 and 20 – 50 KeV energy bands, respectively. The *rightmost image* is after the event.

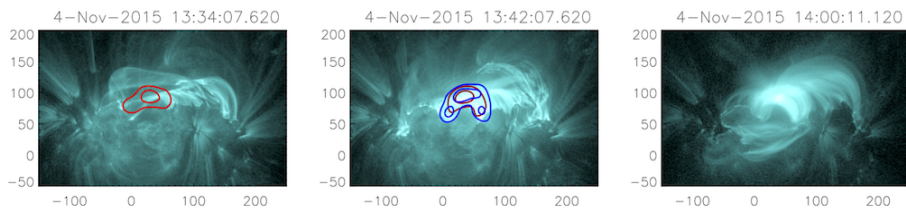


Figure 8. Snapshots showing the evolution of Event 3 in AIA 131 Å filtergrams. Red and blue lines are contours from RHESSI X-ray images reconstructed during the early rise phase (*left*) and peak (*middle*) in the 6 – 12 and 20 – 50 KeV energy bands, respectively. The *rightmost image* is after the event.

For Events 1 and 2, most of the intensity appeared off-limb. In order to analyse the off-limb kinematics of Event 1, we extracted intensity traces from lines at several angles originating from the active region as indicated in Figure 10a. For one angle, intensity traces at successive times were stacked to produce a distance–time map. The distance–time maps were made for the 171, 193, and 211 Å filters and then combined in the usual RGB format so activity at the three wavelengths may be represented simultaneously in a single map. Panel b shows one such distance–time map for the -60° trace indicated by the red line in Panel a. The map reveals that the eruption along this direction was composed of several distinct features, including a bright yellow EUV front that becomes visible at 03:22 UT and reaches a speed of 990 km s^{-1} ; this was followed by escaping filamentary material with a speed of 255 km s^{-1} and finally the failed filamentary eruption which starts to fall back to the solar surface at 03:45 UT. Traces taken along angles from -60° to -30° show similar behaviour, while traces along angles from -20° to 0° only show the bright yellow front (no following filament), propagating at speeds of $\sim 800 \text{ km s}^{-1}$ in this direction. No radially propagating feature could be traced in the 10° trace or above this angle.

The distance–time analysis performed for Event 2 is shown in Figure 10c and d, where the example distance–time map is from the -70° trace as indicated in Panel c. Again several eruption-related features may be identified, the fastest of which is a bright EUV front that begins just after 12:00 UT and propagates with

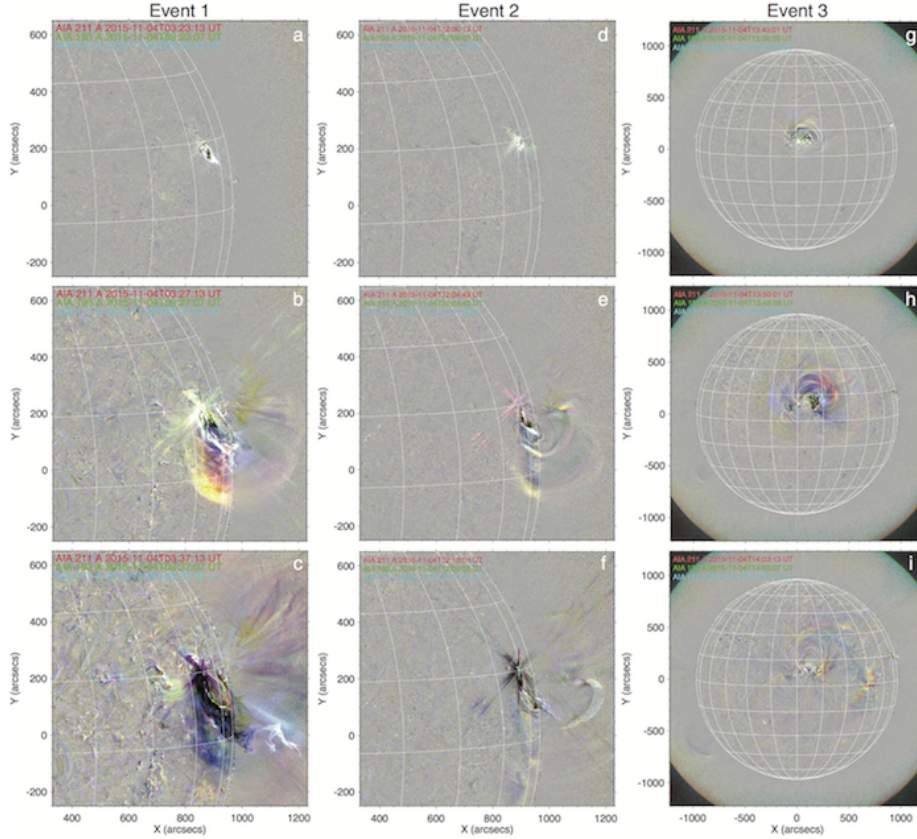


Figure 9. Summary of eruption evolution for the three events occurring on 4 November 2015. (a)–(c) Event 1, beginning with a compact flare-brightening at (N14,W65) at 03:23 UT, followed by a filament eruption and a EUV front which largely propagate in a southwesterly direction. The filament eruption partly failed, with material falling back to the surface and erupting outwards. (d)–(f) Event 2 has similar evolutionary characteristics to Event 1, beginning with a flare-brightening from the same active region and a filament eruption. The filament is surrounded by two distinct yellow structures, the outer one being an EUV front, while the inner one develops into a loop-like feature seen in panel (f). The filament eruption is smaller than Event 1 and largely failed. (g)–(i) Event 3 occurs at disk center, beginning with a brightening of coronal loops and the propagation of a diffuse EUV front in the northwest direction.

a speed of 1030 km s^{-1} . This is followed by a much slower front (most likely the feature which develops into a coronal loop in the images) and then non-erupting filamentary material – the failed filament eruption is not as pronounced as Event 1. The same features may be identified in the distance–time maps that are oriented towards the south, *i.e.*, -70° to -30° , while traces at -20° to $+10^\circ$ show only the slow secondary yellow front (loop) propagating at speeds of $\approx 350 \text{ km s}^{-1}$.

EUV waves from Events 1 and 2 were also seen to propagate on the disk, limited to the south to southeast directions. The speed of the wave as it prop-

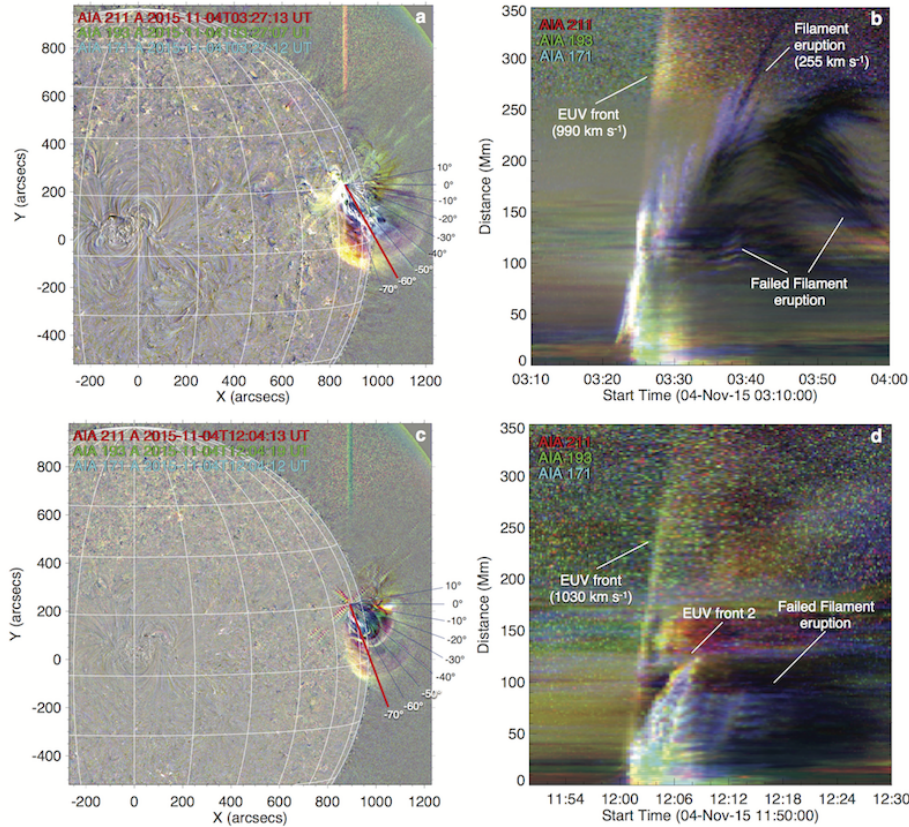


Figure 10. EUV kinematics summary for Events 1 and 2. (a) Snapshot showing the EUV structures. The blue lines that originate at the erupting active region show the directions along which distance-time maps were produced. (b) Distance-time map taken along the red line traced at angle -60° in panel (a), showing the EUV front, filament eruption, and the failed section of the filament eruption. (c) Event 2 eruption in the same format as (a). The line highlighted in red is the trace (-70°) along which the distance-time map shown in panel (d) was constructed. It shows several erupting features including the outer EUV front and the erupting loop.

agated on the disk was measured along the great circle passing the flare (Nitta *et al.*, 2013). The speed was lower on the disk than that measured off-the-limb. It was $\approx 750 \text{ km s}^{-1}$ and $\approx 600 \text{ km s}^{-1}$, respectively, for Events 1 and 2. The EUV wave from Event 3 was diffuse and anisotropic, identifiable only westwards of AR 12443 with the brightest part moving northwestward (Figure 11). The speed in that direction was $\approx 700 \text{ km s}^{-1}$. The EUV wave was seen between 13:40 UT and 13:50 UT, comparable to the period in which Type II bursts were observed (see Section 5). A more detailed analysis of this EUV wave will be given elsewhere.

The early stages of the failed eruptions in the low corona were analysed using SDO/AIA for Events 1 and 2, in order to better understand the CMEs they drove. Figure 12 shows the failed filament eruption for Event 1, using

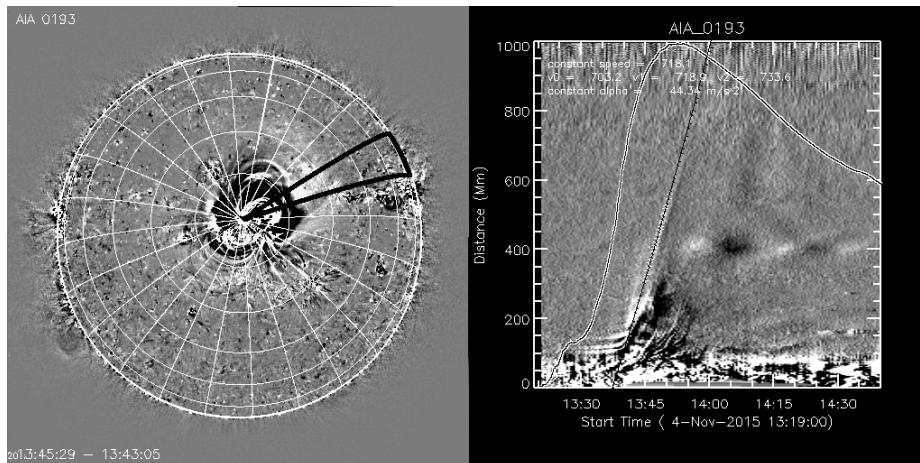


Figure 11. The kinematics of the EUV wave for Event 3. (*Left*): The speed and acceleration are calculated along great circles averaged in $24\ 15^\circ$ -wide sectors that originate at the flare center. (*Right*): Space–time plot of the sector marked in black in the left panel. The normalized GOES 1–8 Å light curve is overplotted using a black line superposed on a broader white curve. Even in running– difference images the wave front is diffuse. The selected sector is one of the few that let us trace the front edge of the wave.

304 Å data from SDO/AIA. The compact flare of Event 1 was followed by a filament eruption toward the Southwest in the plane of the sky, along a curved path that is initially at a small angle to the local chromospheric surface. An EUV front and a weak Moreton wave (identified in movies of H_α filtergrams from GONG and Kanzelhöhe Observatory) accompanied the eruption, propagating both southwards on-disk and in a southwesterly direction off-limb. By 03:37 UT the EUV front had left the AIA field of view and started to dissipate in intensity. While some of the filament was completely ejected, a large portion of it fell back to the solar surface, both towards the active region, and to an area south of the active region. The falling material produced bursts of 304 Å radiation when it hit the chromosphere, presumably from the heating of the plasma.

The motion of the filament material can be analysed quantitatively by studying the location (or distance) of bright or dark features as a function of time along a specified path (McCauley *et al.*, 2015). Taking into account the curved path followed by the erupting material in the bottom panels of Figure 12 leads to the distance–time diagram in the top panel. The linear segment of one fast feature in the top panel corresponds to a speed of $348\ \text{km s}^{-1}$, with others having top speeds of $\approx 500\ \text{km s}^{-1}$. The downwards curvature corresponds to acceleration sunwards. The parabolic line corresponds to an acceleration of $0.22\ \text{km s}^{-2}$, agreeing very closely with the Sun’s predicted gravitational acceleration (of $0.27\ \text{km s}^{-2}$) at this distance. Note that there is a difficulty understanding the paths taken by the erupting and falling material: if the curved eruption path is interpreted as following the local magnetic field, then the more vertical path taken by the falling matter suggests either that the field direction has changed substantially or that the falling matter does not follow the field lines.

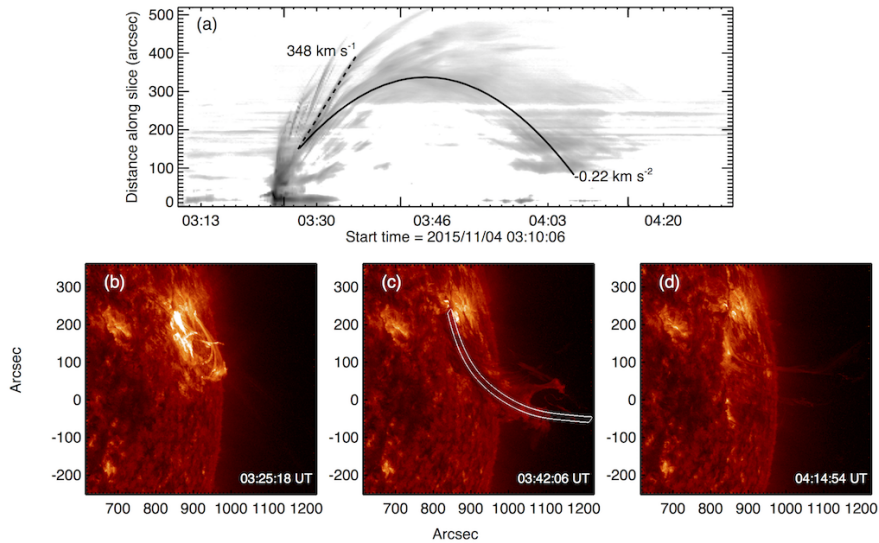


Figure 12. Filament eruption kinematics from 304 Å SDO/AIA observations of Event 1. (a) Background-subtracted distance-time plot using the curved trajectory in (c). (b)–(d) Snapshot 304 Å SDO/AIA images at three times. The filament is ejected behind and somewhat slower than the EUV wave, and the failed eruption material returns at slightly lower than gravitational acceleration (0.27 km s^{-2}).

4.2. CMEs for Events 1 and 2

Figure 13 shows the evolution of the first two CMEs in the field of view of the C2 camera ($2 - 6 R_{\odot}$) of the *Large Angle and Spectrometric Coronagraph* (Brueckner *et al.*, 1995, LASCO) on board SOHO. Figure 13a is a direct image from LASCO C2 taken at 00:00 UT on 4 November, where the black contours identify the location of the coronal streamers shaping the pre-event topology of the solar corona. Figures 13b–i are difference images at the indicated times and the white contours indicate the location of the coronal streamers identified in Figure 13a. Figures 13b–c at 02:24 UT and 03:12 UT show an unrelated CME (first seen in LASCO C2 at 02:00 UT) that occurred prior to the events under study. This preceding CME came from a small sigmoid eruption from the decaying AR 12441, which was downgraded to a non-numbered region on 4 November.

Figures 13d–f (second row) show the evolution of the CME associated with Event 1, which was first seen in C2 at 03:48 UT. It propagated mostly within the streamer, and by 05:00 UT it broke into different parts. In fact it is extremely difficult to see it in the field of view of LASCO C3 ($3.5 - 30 R_{\odot}$). The weak and fragmented appearance of this CME may be due to its propagation within the coronal streamer. The estimated plane-of-sky speed at a position angle of 280° (*i.e.* 10° above the equatorial plane) was $328 \pm 8 \text{ km s}^{-1}$.

Similarly, Figures 13g–i (third row) show the evolution of the CME associated with Event 2. This CME was first seen in the LASCO/C2 field of view at 12:36 UT. It propagated within the streamer and by 14:36 UT, just before

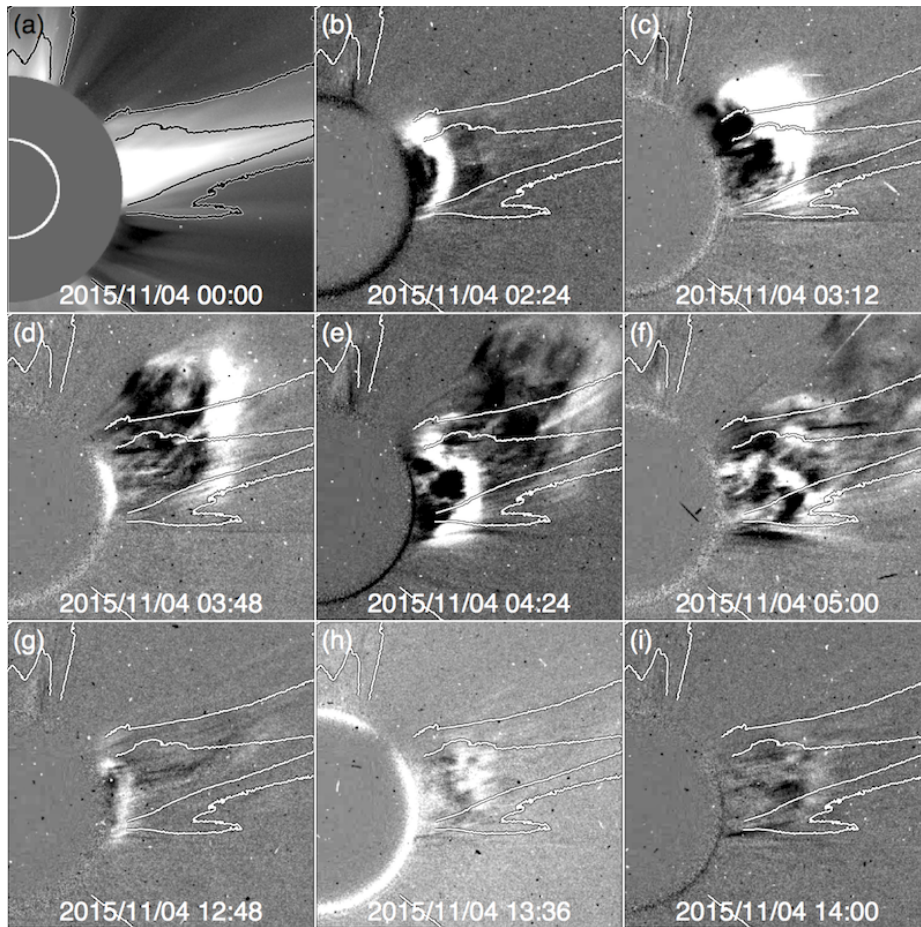


Figure 13. The evolution of the CMEs for Events 1 and 2, as seen by the LASCO instrument's C2 camera onboard SOHO. See text for details.

the CME from AR 12443 associated with the Event 3 occurred, it was already very difficult to see in the LASCO C2 images. The estimated plane-of-sky speed at a position angle of 280° (*i.e.* 10° above the equatorial plane) was $252 \pm 14 \text{ km s}^{-1}$.

Although the CMEs associated with Events 1 and 2 were initially impulsive without a clear driver, the magnetic structure in which they propagated (*i.e.* the coronal streamer) might have played a role in their fast weakening, ragged structure, and rapid decay. Similarly, the generation of the metric Type II emissions observed (see Section 5) may have been favored by the closed magnetic field structure at the base of coronal streamer encountered by these two weak CMEs (*e.g.* Kong *et al.*, 2015). As shown below, the fast decay of the CMEs did not favor the production of interplanetary Type II emissions.

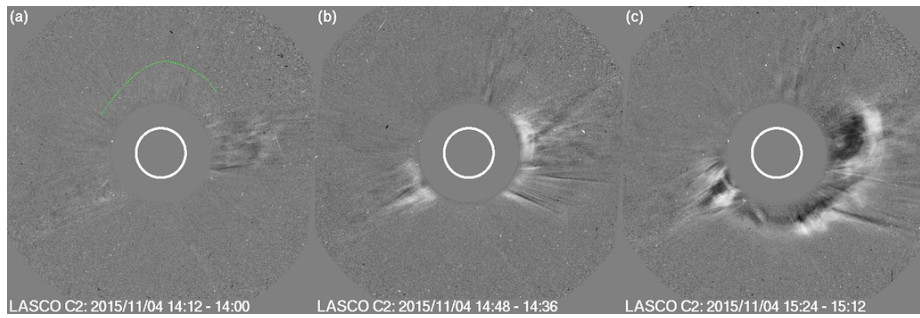


Figure 14. The evolution of the CME for Event 3. See text for detail.

4.3. CME for Event 3

According to the CDAW LASCO CME catalog (http://cdaw.gsfc.nasa.gov/CME_list), the CME associated with Event 3 first appeared at 14:48 UT in the West to Northwest directions and then developed into a full halo CME; see Figures 14b and c, respectively. Its average plane-of-the-sky speed in the LASCO field of view was $\approx 580 \text{ km s}^{-1}$ with a slight acceleration that led to a speed of $\approx 620 \text{ km s}^{-1}$ at the last measurable height of $15 R_{\odot}$. Note that the CME front is far from smooth, suggestive of multiple flux ropes or several distinct erupting structures contributing to it. Close examination of the LASCO difference movies reveals a very diffuse front, indicated by a green curve in Figure 14a, that moves northward between 14:00 UT and 14:24 UT. The average speed in the image plane was $\approx 1200 \text{ km s}^{-1}$.

5. Coronal and Interplanetary Radio Bursts

Figure 15 shows a summary of all radio bursts occurring on 4 November 2015 during the period 03:00–16:00 UT in the domain 0.01 – 1000 MHz. The figure consists of a mosaic of plots from the Wind/WAVES, Learmonth, Culgoora, Orfées, Nancay Decametric Array (referred to as NDA below), and Callisto (Bleien, Mauritius, and Gauribidanur) spectrographs.

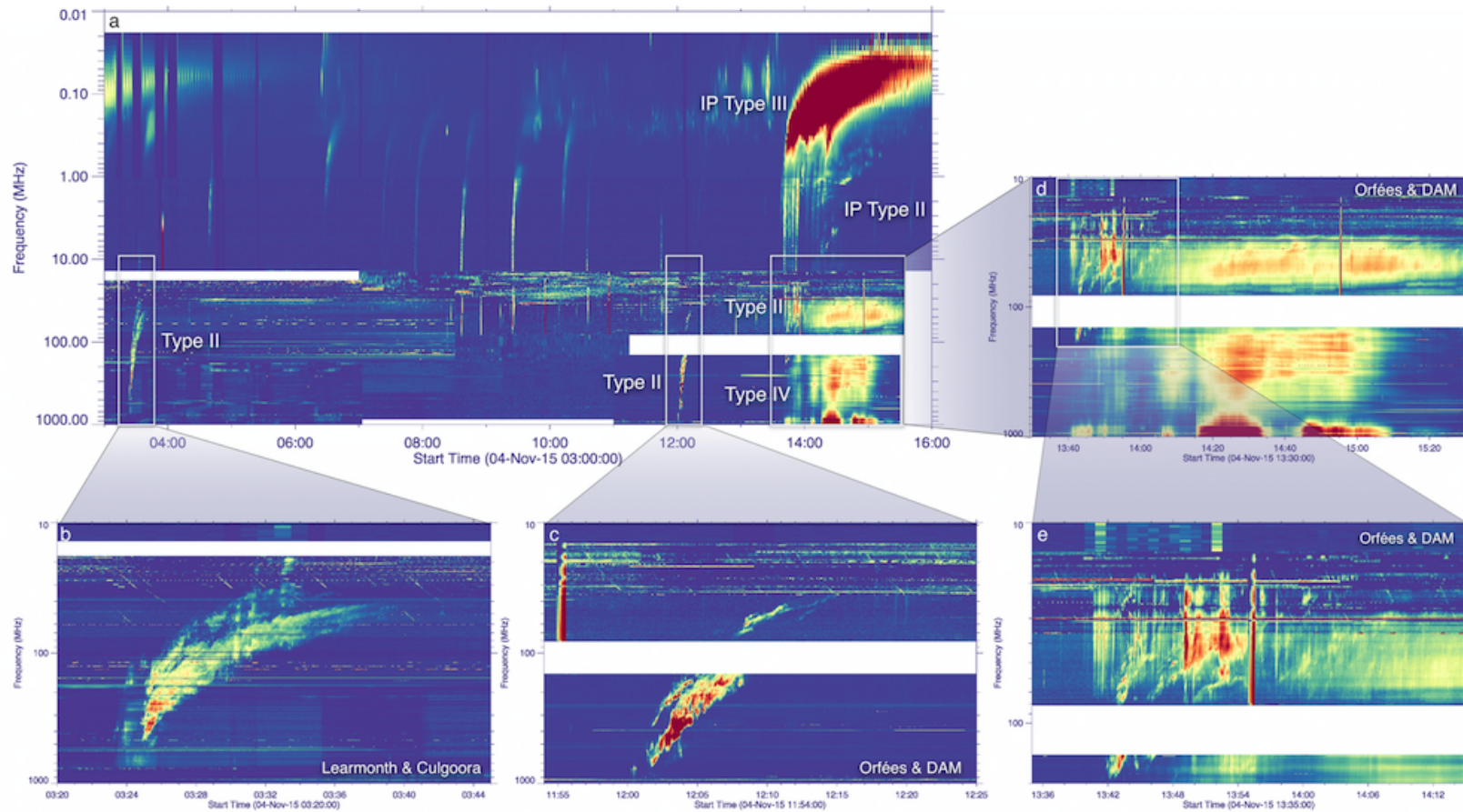


Figure 15. (a) Summary of all radio dynamic spectra for the events on 4 November 2015. Constructed from a mosaic of *Wind*/WAVES, Learmonth, Culgoora, Orfées, Nan cay (NDA), and Callisto (Bleien, Mauritius, and Gauribidanur). (b) Event 1 was associated with a metric Type II radio burst that began at ≈ 600 MHz that does not extend obviously below 10 MHz. Weak Type III radio bursts occur prior to the Type II burst and then start at the same frequency as the Type II near 03:30:15, 03:31:15, and 03:33:00 UT. These are associated with a small interplanetary Type III observed by *Wind*/WAVES in (a). (c) Event 2 was associated with strong metric Type II emission, beginning at ≈ 800 MHz. No interplanetary Type IIs or IIIs were observed for this event. (d)-(e) Event 3 was associated with at least three metric Type II bursts (see the details in (e)), multiple metric Type III bursts, and a Type IV burst over the band 20 – 700 MHz. These metric events led to an interplanetary Type II and numerous interplanetary Type IIIs.

From Figure 15a, the three events start near 03:25 UT, 12:00 UT and 13:40 UT. All three events have strong and complex metric Type II radio bursts, all with multiple lanes and both fundamental and harmonic emission. The metric Type III characteristics differ strongly between Events 1 and 2 on the one hand, and Event 3 on the other hand. Unlike the other two, Event 3 has a strong Type IV burst.

5.1. Event 1

Figure 15b is an enlargement of Event 1’s dynamic spectrum using Learmonth and Culgoora data. It is complex, showing evidence for multiple lanes and several time-varying fundamental and harmonic bands. The strongest harmonic emission starts near 450 MHz, an unusually high frequency, at \approx 03:25 UT and drifts to \approx 50 MHz over period of \approx 12 minutes, although evidence for weaker Type II-like emission exists near 800 MHz near 03:24 UT. Weak fast-drifting signals from near 03:23:30 to near 03:25 UT at frequencies \approx 100 – 800 MHz are likely Type III bursts. They are the low-frequency counterpart of the impulsive microwave burst (Figure 4). These bursts are cut off near 100 MHz, with no counterpart in the high corona and interplanetary space. Similar Type III bursts start near 03:30:15, 03:31:15, and 03:33:00 UT close to the frequency of the harmonic Type II burst and drift to lower frequency. These latter bursts might be interpreted in terms of SA events (Cane *et al.*, 1981; Cane and Stone, 1984; Bougeret *et al.*, 1998; Reiner and Kaiser, 1999), where SA variously stands for Shock Accelerated (Cane *et al.*, 1981; Cane and Stone, 1984) or Shock Associated (Bougeret *et al.*, 1998) or complex Type III-like (Reiner and Kaiser, 1999) events, as discussed further below. They are most likely related to the weak interplanetary Type III that is visible in expanded views of the *Wind*/WAVES data near these times in the restricted frequency range 8 – 14 MHz and then becomes clearly visible in the approximate frequency range 150 – 600 KHz and period 03:40 - 03:50 UT. The fact that there is no strong Type III emission from coronal (RSTN) to interplanetary (*Wind*/WAVES) frequencies for this event, despite the evidence for efficient electron acceleration from X-ray and microwave observation (see Section 3), suggests that either most of the accelerated electrons did not reach open magnetic field lines (Axisa, 1974; Klein, Trotter, and Klassen, 2010), or that they were radio-quiet along open field lines (Li and Cairns, 2012, 2013). The observation of SEP electrons for Event 1 (see Section 7.1) provides strong evidence for the latter interpretation. The multiple lanes of Type II emission, possibly with band-splitting as well, indicate either i) that a single shock has multiple source regions with different densities simultaneously producing observable radio emission or ii) that more than one shock exists and produces radio emission in distinct regions with different densities.

5.2. Event 2

Figure 15c shows Event 2’s Type II radio burst, observed using Orféés and NDA. Overall, this burst was much weaker than the other two. It is also complex, with evidence for multiple lanes that have different frequency-drift rates and

sometimes overlap. The event has clear fundamental and harmonic structure, starting at the unusually high frequencies of ≈ 350 MHz and ≈ 700 MHz near 12:01:30 UT, and drifts to 30 MHz over a period of 12 minutes. Interestingly, the Type II event starts with quite an intense harmonic that diminishes quickly. By the time the event enters the NDA frequency domain ($\approx 10 - 80$ MHz) it has faded to primarily a weak fundamental band, again with evidence for multiple lanes, and perhaps some very weak harmonic emission. There was no significant interplanetary Type II activity associated with this radio event or the faint microwave burst seen approximately 12:00 – 12:04 UT (Section 3). There was also no discernible Type III emission at coronal or interplanetary frequencies, a small difference from the weak Type III emission for Event 1, again interpretable in terms of electrons not being released onto open field lines or not having the right properties to produce observable radio emission.

5.3. Event 3

Figures 15d and e show enlargements of the radio bursts of Event 3 above 10 MHz. This was by far the most complex of the three radio burst events. It begins with Type III bursts starting shortly before the Type II burst appears. These initial Type IIIs are easily seen near 1 GHz and below 80 MHz, while the first Type II emission begins near 13:42 UT and 200 MHz. This Type II mainly exists at NDA frequencies and shows very complex and sporadic bands of emission. Indeed an unusually large number of multiple lanes (not distinguishing between bands and split-bands) are identifiable (at least 6 and perhaps up to 11 or beyond depending on the observer's definition) and for an unusually long period, from 13:42 UT near 200 MHz until about 14:08 UT near 30 MHz. In addition a broadband, long-lasting, Type IV radio burst exists between about 30 and 1000 MHz, typically at higher frequencies than the Type II burst and extending long after the Type II burst has ceased. The Type IV burst is particularly intense at frequencies above 700 MHz, extends to unusually low and high frequencies, and appears to show strong vertically-aligned fine structures, particularly above the NDA domain for 13:50 – 13:56 UT and after about 14:00 UT. More detailed analysis is required to determine whether or not the fine structures show the increase of duration with decreasing frequency that characterises Type III bursts. The Type IV emission also shows pulsations in intensity on timescales of minutes.

Type III bursts are also observed during much of Event 3, starting with a strong set in the period 13:40 – 13:42 UT before the Type II emission starts and then continuing intermittently before some more intense events occur at frequencies below the Type II burst during the period 13:49 – 13:54 UT. These latter events intensify at the frequency of the Type II burst, suggesting a physical association, but they may also have counterparts at frequencies above ≈ 150 MHz in the Orféus domain.

5.4. Interplanetary and *In-Situ* Observations

Returning to Figure 15a for Event 3, the interplanetary extensions of the metric Type IIs are clearly present until at least 16:00 UT and a frequency of 500 KHz,

but plausibly until 17:15 UT and 200 KHz. Fundamental and harmonic pairs are evident. Furthermore, multiple lanes are present again, with one restricted to above 4 MHz before about 14:30 UT and the limits on the other set described previously.

Multiple distinct interplanetary Type IIIs are evident in the frequency range 400 kHz to 14 MHz of Figure 15a, as detailed more below, merging into an extended burst below 200 kHz that has little structure (with this color bar) and lasts until after 16:00 UT. This type of unusually long and bright group of Type III bursts is often called a Type III-L event (Cane, Erickson, and Prestage, 2002). Note that the two sets of metric Type IIIs discussed above connect to multiple individual interplanetary Type IIIs and the merged burst below 200 kHz.

Next we analyse the *Wind* radio and plasma-wave data to constrain observationally the presence or absence of energetic electrons that reach 1 AU near Earth. Figure 16 shows a partial RAD1 dynamic spectrum ($\approx 5 - 250$ kHz) for 4 November 2015, while Figure 15 shows the entire RAD1 (to 1 MHz) and RAD2 ($\approx 1 - 14$ MHz) domains. Figure 16 primarily shows some weak intermittent individual Type IIIs from 13:30 – 13:50 UT and then a saturated, longlasting emission that might be identified as a Type III-L burst (Cane, Erickson, and Prestage, 2002). However, Figure 15a clearly shows multiple individual Type IIIs below ≈ 1 MHz throughout the approximate period 13:30 – 14:30, although above about ≈ 4 MHz separation into two groups appears reasonable. Evidence thus exists for Type III electron beams that are radio-quiet above ≈ 4 MHz but radio-loud below ≈ 1 MHz.

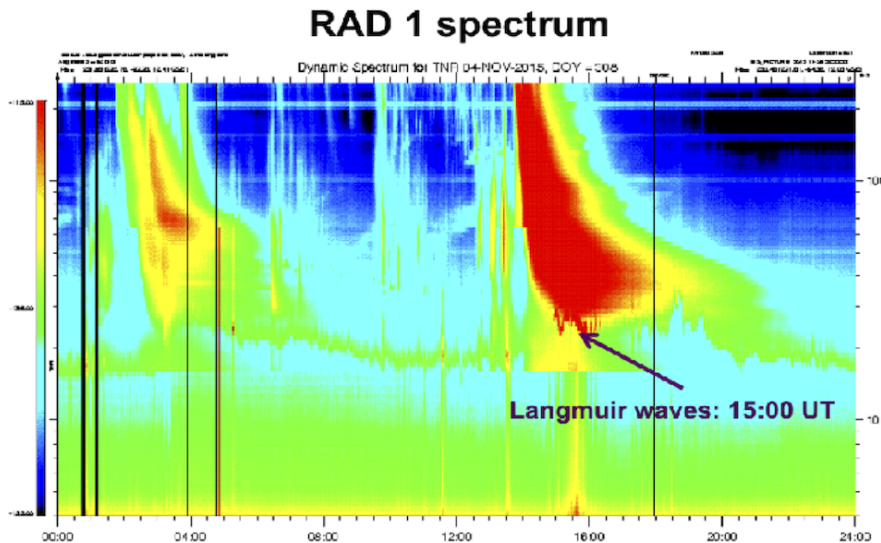


Figure 16. *Wind* WAVES/RAD1 dynamic spectrum for 4 November 2015.

Figure 16 shows direct evidence for generation of Langmuir waves associated with the multiple interplanetary Type III bursts present. This evidence is the intensification of the “plasma line” near f_{pe} , corresponding to the green line near

20 kHz from 08:00 to 14:00 UT that becomes red in the approximate period 15:00 – 16:30 UT and ranges in frequency between about 20 and 30 kHz. Thus, during at least this latter period it appears that Type III electrons are present and unstable to the growth of Langmuir waves.

6. Magnetic Field Configuration and Interplanetary Conditions

6.1. Coronal Magnetic Fields and Heliospheric Connectivity

Figure 17, based on the PFSS model, as adopted by Schrijver and De Rosa (2003) and implemented in *SolarSoft*, predicts that the open field lines that reach the ecliptic plane at the source surface, placed at a heliocentric distance of $2.5 R_{\odot}$, come from three places: the western periphery of AR 12445 (negative polarity – purple lines), a coronal hole to the Southeast of the region (positive polarity – green lines), and the eastern periphery of AR 12443 (positive polarity). Similar results were obtained (not shown) by the National Solar Observatory using its PFSS model with GONG magnetogram data.

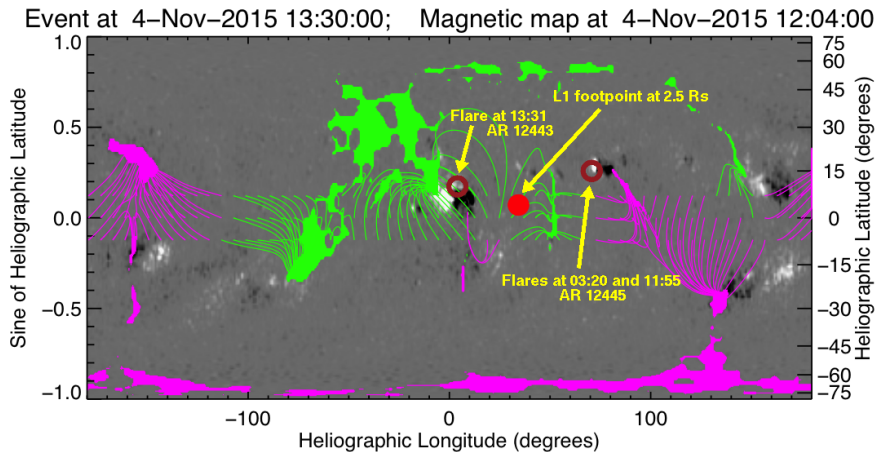


Figure 17. Predictions of a PFSS model with HMI photospheric magnetic field data for a synoptic magnetic map at the photosphere in Carrington coordinates around the time of the second flare, except that the Carrington longitudes are translated to Earth-view longitudes. The *open circles* show the photospheric locations of the flares with solar rotation corrected. The *red circle* is the footpoint of the magnetic field line traced from L1 to the source surface at $2.5 R_{\odot}$ using Wind spacecraft velocity data and the Parker spiral (second method in the text). Open field regions are marked in two colors (*green*: positive, and *pink*: negative).

Instead of using the PFSS model with photospheric magnetic field data, we can start at the Earth and use the solar wind speed observed by the *Wind* spacecraft and the Parker spiral model for $\mathbf{B}(\mathbf{r})$ to estimate the heliographic coordinates on the source surface of the field line that crosses the Earth at a

given time. From there, we can map the field line to the photosphere using the PFSS model. Using this approach, the field line that was connected to the Earth at 12:00 UT on 4 November was rooted in the coronal hole between AR 12443 and AR 12445, and its polarity matches that observed at L1. Using a more sophisticated heliospheric MHD simulation model (provided by Predictive Science, Inc.) shows that the footprint of the Earth-connected field lines became rooted in AR 12443 at 4 November 00:00 UT. This connection lasted until the next day. A note of caution is that the first eruption may distort the magnetic field configuration (and the other plasma structures) from the PFSS and Predictive Science, Inc. predictions for the second event.

A different approach altogether is to extrapolate 1 AU *in-situ* solar wind observations back in time and space. Figure 18 maps the large-scale magnetic field lines and solar wind velocity streams in the solar equatorial plane, extending up to a distance of 2 AU and constructed using a 2D solar wind model (Schulte in den Bäumen, Cairns, and Robinson, 2011, 2012) and the approach of Li *et al.* (2016). The process involves fitting *Wind* measurements of B_ϕ , B_r , and v_r at 1 AU to an analytic model, permitting calculation of these quantities and the plasma density from 1 AU to an inner boundary (nominally at the photosphere). The analytic model assumes the magnetic field to be frozen-in to the plasma, the wind sources to be constant over a solar rotation (so that the wind and its magnetic field lines form a constant pattern that rotates with the Sun, thereby not modelling CME effects properly), the flow speed to be constant along each streamline, and the plasma to corotate with the Sun at the inner boundary. The model and fitting procedure allow the magnetic field to be non-radial at the inner boundary.

On 4 November, Earth is near the bottom of Figure 18. The field line that reaches Earth on 4 November leaves the Sun about 45° westward from the Sun – Earth line. It is quite closely Parker-like, albeit longer, but its neighbors are not: the nearest eastward field line is directed almost radially near 1 AU (and so lies at an angle of order 45° to the nominal Parker direction) and so initially moves westward rather than eastward, while the nearest westward field line does not proceed far Sunward due to it entering a region with magnetic field close to zero (note the opposite directions for the lines that reach 1 AU between 2 and 4 November), and the next westward field line is part of a loop disconnected from the Sun that does reach 0.1 AU. These aspects suggest that electrons produced by Events 1 and 2 very close to the west-limb source (whether flare- or shock-produced) should not be magnetically connected to Earth on 4 November, unless there is substantial scattering or the acceleration region has a large angular width. Semi-quantitatively, it appears that scattering through $25 - 60^\circ$ of longitude is needed, on considering the location of AR 12445 on the Sun and comparing the angular distances at 1 AU between the corresponding field lines that connect to Earth’s locations for 31 October to 2 November with the field line for 4 November. However, the disk center source for Event 3 should be magnetically connected to 1 AU about 15 degrees eastward of Earth (the angular distance between the field lines that connect to Earth on 4 and 5 November). Thus, Event 3 should be better magnetically connected than Events 1 and 2 but still not well connected.

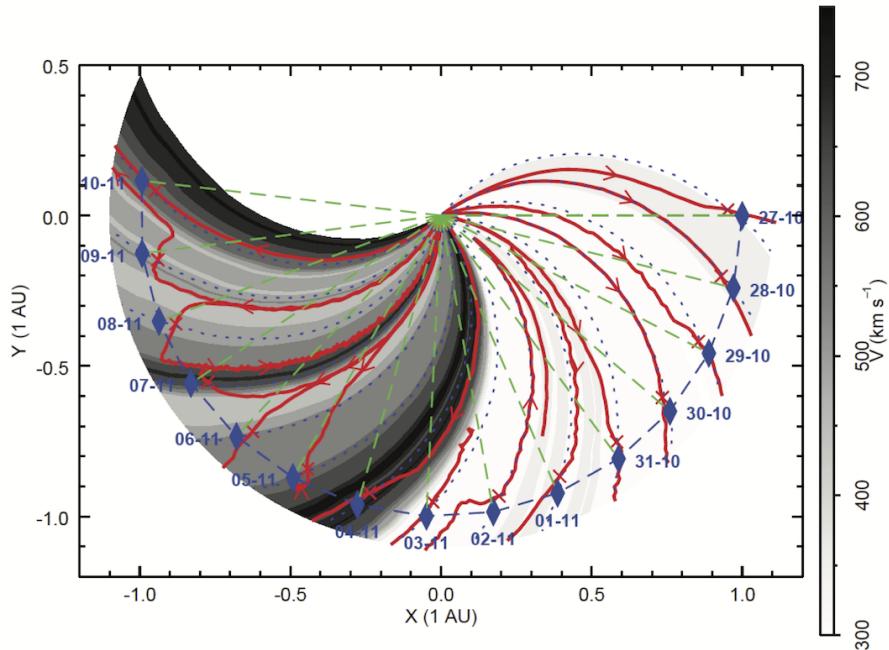


Figure 18. Magnetic map in the solar equatorial plane for the interval 27 October to 11 November 2015, calculated using *Wind* spacecraft data and the approach of Li *et al.* (2016). *Dashed blue lines* show the nominal Parker spirals while *blue diamonds* show the position of the Earth on specific days. *Dashed green lines* show the Sun–Earth line for each day.

6.2. Interplanetary Plasma and Field Observations

Figure 19 overviews the in-situ plasma, magnetic field, and particle observations in the vicinity of the Earth from 2 November (DOY 306) to 9 November (DOY 313) 2015. The figure shows from top to bottom: (a) 175 – 315 KeV electron intensities and (b) 1.9 – 4.8 ion intensities observed by ACE/EPAM (Gold *et al.*, 1998), the solar-wind proton (c) speed, (d) density, and (e) temperature observed by ACE/SWEPAM (McComas *et al.*, 1998), the (f) magnetic-field magnitude and (g,h) field angles in Radial Tangential Normal (RTN) coordinates, and (i) B_z component in the Geocentric Solar Ecliptic (GSE) frame observed by ACE/MAG (Smith *et al.*, 1998), and the (j) Dst, (k) AE, and (l) Kp geomagnetic activity indices. The red line in the temperature plot corresponds to the solar-wind proton temperature predicted for non-ICME periods using the solar wind speed and expression of Elliott *et al.* (2012). The vertical solid lines mark interplanetary shock passages observed in-situ and shaded regions indicate ICME periods identified by I.G. Richardson and H.V. Cane (<http://www.srl.caltech.edu/ACE/ASC/DATA/level3/icmetable2.html>).

The enhanced magnetic field and density region observed on 3 November corresponds to a stream-stream interaction region, produced when the high-speed stream (speeds $v_{sw} \approx 700 \text{ km s}^{-1}$) observed during 3–4 November compressed

the preceding slow solar wind ($v_{sw} \approx 320 \text{ km s}^{-1}$). The first vertical line corresponds to a reverse shock associated with that CIR. This shock was coincident with the local peak of the energetic proton intensity increase associated with the CIR.

A second interplanetary shock was observed on 4 November 03:24 UT, shortly before the onset of a weak solar electron event (see first label “SEP” in the top panel). An interval with ICME signatures was observed 10.8 hours after this shock, as indicated with the first shaded area from 14:10 UT to 19:26 UT in Figure 19. These signatures included smooth magnetic-field rotation, low temperature and bi-directional solar-wind electron flux (the latter not shown). No significant increase of the magnetic-field magnitude was observed, suggesting that the spacecraft crossed close to one of the flanks rather than near the central part of the ICME. A second SEP event, showing electron and proton increases, was observed when the spacecraft was inside the ICME. The connection of these first two SEP events to Events 1–3 is discussed in detail in the next Section. Here we emphasise that the two shocks just discussed reach 1 AU far too early to be associated with the three solar events on 4 November 2015.

We add for the purpose of the space weather discussion in Section 8 that a third interplanetary shock was observed on 6 November 17:35 UT, followed by an ICME covering the period 7 November 06:00 UT to 8 November 16:00 UT. This ICME showed very clear signatures, and it was likely the interplanetary counterpart of the CME ejected on 4 November in association with Event 3. The time elapsed is 52 hours and the averaged speed is 800 km s^{-1} . This average transit speed lies between the two plane-of-the-sky estimates of ≈ 600 and 1200 km s^{-1} estimated for the associated CME in Section 4.3.

7. SEPs

7.1. SEP Observations

Figure 20 shows energetic particle, plasma flow, and magnetic field observations during 4 November 2015. From top to bottom the figure shows: (a) energetic electron intensities observed by SOHO/EPHIN (Müller-Mellin *et al.*, 1995) at three energy bands, (b) energetic proton intensities observed by ACE/EPAM, SOHO/EPHIN and SOHO/ERNE (Torsti *et al.*, 1995) at five energy bands between 1 and 32 MeV, solar wind (c) speed, (d) magnetic field magnitude, and (e,f) magnetic field angular coordinates observed by ACE during 4 November. The shaded area corresponds to the first ICME shown previously in Figure 19. The arrows in the first two panels mark the times of X-ray flares associated with the three events under study. During this period, the SOHO spacecraft was rotated 180 degrees from its nominal pointing, meaning that its particle instruments were pointing perpendicular to the nominal Parker spiral direction and missed the field-aligned particles expected to arrive first.

Two electron increases, with 0.25 – 0.74 MeV onset times at 04:11 UT ± 2 minutes and 14:19 UT ± 2 minutes, were observed. The first increase, associated with Event 1, was clearly observed by the EPHIN instrument and the

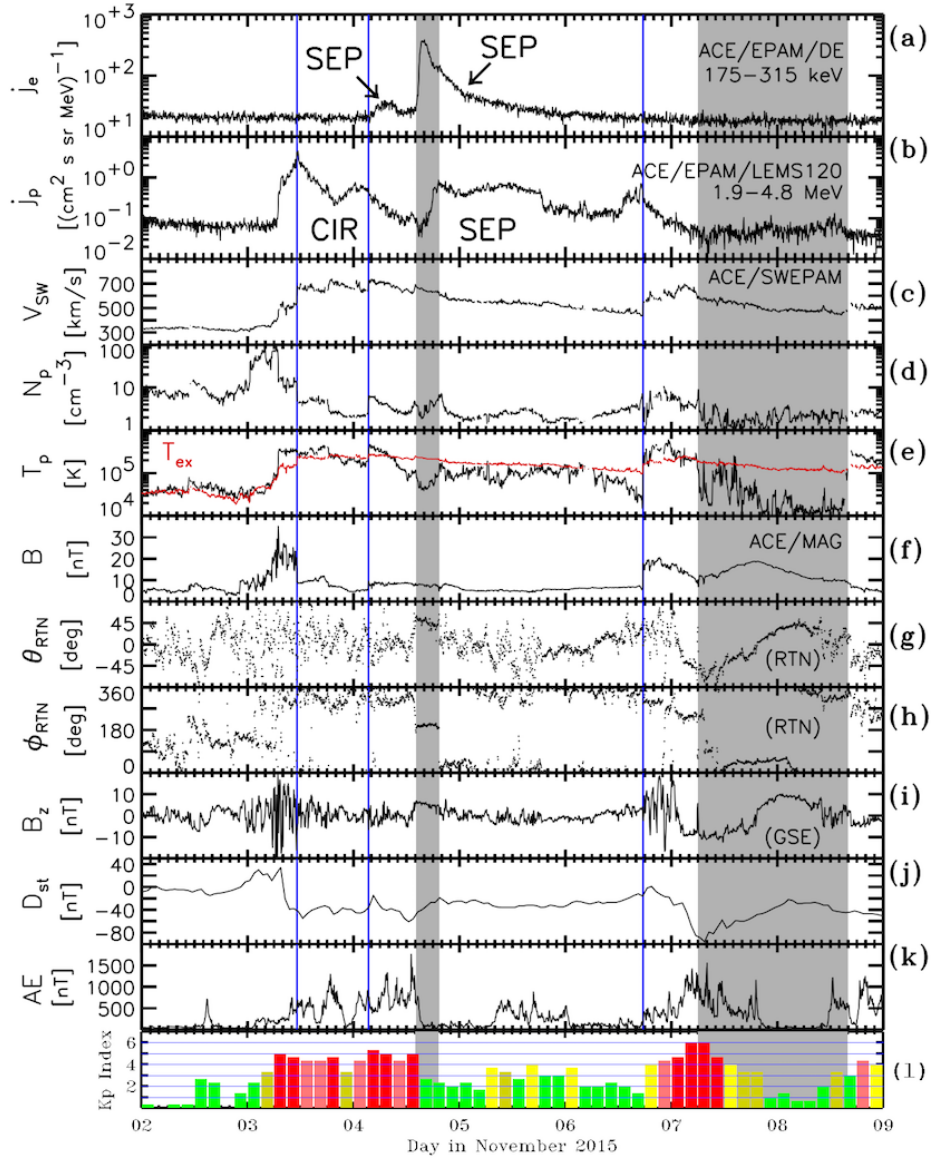


Figure 19. Overview of in-situ observations: (a) 175 – 315 KeV electron intensities, (b) 1.9 – 4.8 MeV ion intensities, (c) solar wind proton speed, (d) solar wind proton density, (e) solar wind proton temperature, (f) magnetic field magnitude, (g) magnetic field latitudinal angle, (h) magnetic field azimuthal angle, (i) B_z , the z GSE component of the field, (j) Dst index, (k) AE index, and (l) Kp index. Blue vertical lines identify shocks while shaded areas correspond to ICME periods. See text for details.

deflected electron channels of ACE (Figures 19 and 20). The second electron increase, associated with Event 3, showed higher intensities than the first electron increase and was accompanied by energetic protons reaching energies up to 60 MeV. Both the electron events and the ion event showed clear velocity dispersion.

The electron event 1 was not accompanied by an increase of the proton intensity, possibly because it was masked by the decaying proton intensity associated with the prior CIR. The small proton increase starting at 12:00 UT on 4 November, seen at the higher-MeV energies (see the blue curve in the second panel of Figure 20), started too early to be associated with Event 2. Therefore, there was no significant in-situ particle increase associated with Event 2. (Interestingly, however, modeling presented in Section 7.3 below suggests that this small proton event could be due to protons accelerated in Event 1 once its shock and CME are well away from the Sun.) During the period under analysis, there were no observations available from STEREO-B (communications with the spacecraft stopped in October 2014). STEREO-A was affected by reduced data return during the pass through solar conjunction, but the beacon data available show that the two SEP increases observed at L1 and described in Figures 19 and 20 were not observed by STEREO-A (at that time located at a heliographic longitude of ≈ 168 degrees). Thus the observed SEP electron events do not cover 360° of heliolongitude at 1 AU.

Figure 21 shows the intensities and abundance ratios of multiple energetic ions observed by ACE/EPAM, ACE/ULEIS and SOHO/EPHIN between November 2 and November 9 in 2015. Specifically the figure provides data for protons, helium (technically both ^4He and ^3He , although usually the fraction of ^3He is expected to be negligible), carbon, and oxygen. The shaded areas correspond to ICME periods. While hypothetical SEPs ions from Event 1 might be masked by the CIR-associated increase starting on November 3, all of these species showed clear increases associated with Event 3. The He/H ratio remained close to 0.1 during the whole of Event 3, which corresponds to the typical values found during impulsive (flare-associated) SEP events (see, *e.g.*, Reames 1999). The C/O flux ratio clearly separates the periods with CIR- and SEP-related energetic particles, as found previously (Mason and Sanderson, 1999), providing additional arguments against Events 1 and 2 producing significant SEP ions. Note that the composition signatures of gradual and impulsive events can sometimes be blurred (Cohen, 2006, *e.g.*), as apparently found here.

7.2. Electron Anisotropy Observations and Modeling of SEPs related to Event 3

The electron data above 250 KeV in Figure 20 show only a single onset for Event 3. However, at the lower energies presented in Figures 22 and 23 the electron event has a first peak approximately ten minutes after the onset, followed by a flat interval and then a second major increase of the particle intensity. Furthermore, analyses presented next of *Wind*/3DP sectorized data show two clear episodes of velocity dispersion during the rising phase of the two peaks. (*SOHO*'s orientation prevents similar analyses for this period.) This two-step electron rise

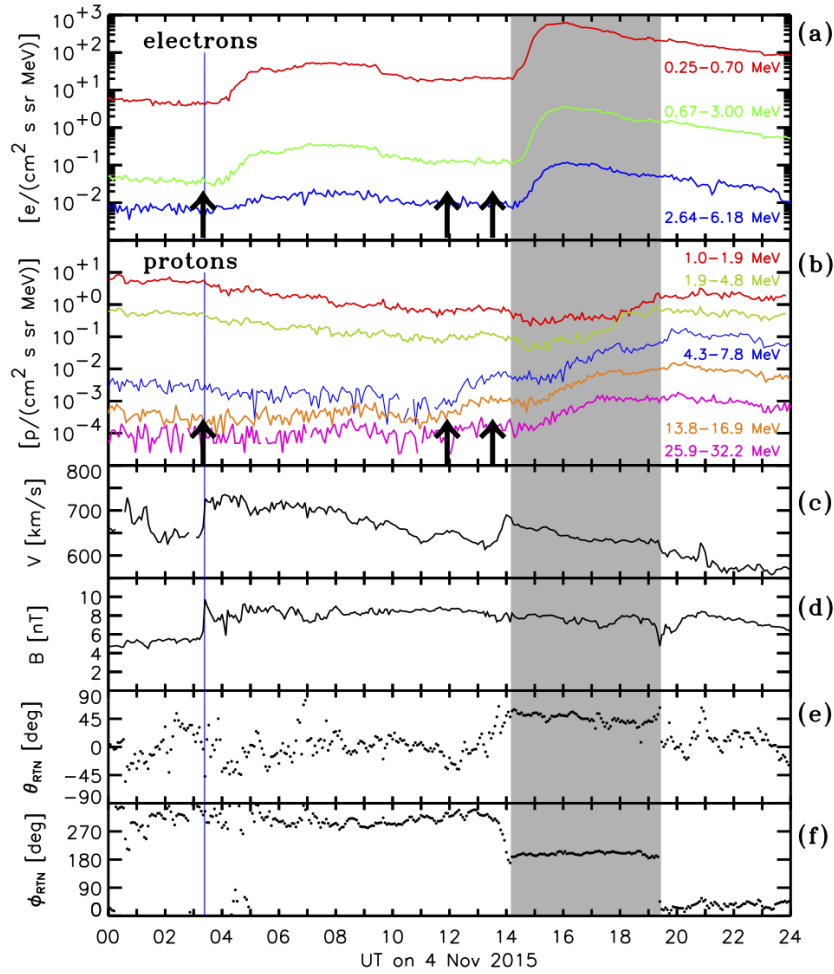


Figure 20. Energetic electron and proton, solar-wind speed and magnetic-field vector observations during 4 November 2015, from instruments on SOHO and ACE at L1. *Thick vertical black arrows* mark the start times of Events 1-3.

is unlikely to be due to local effects because it was observed by both the *Wind* and *ACE* spacecraft, at that time separated by 130 Earth radii and both immersed in the ICME and observing a steady field orientation.

Figure 22 shows the pitch-angle distributions of 82 – 135 KeV electrons observed by *Wind*/3DP in association with Event 3. During the rising phase of the two peaks, *Wind*/3DP observed pitch-angle distributions peaking at small pitch-angles, indicating a good magnetic connection to the solar source region. Moreover, the first order anisotropy index shows a double-peak shape in agreement with the two-step increase of the intensities. These observations suggest that the energetic electron event was composed of two successive groups of injections separated by ≈ 30 minutes. Later on, after about 15:00 UT, the non-monotonic evolution of the pitch-angle distributions (*i.e.* the observation

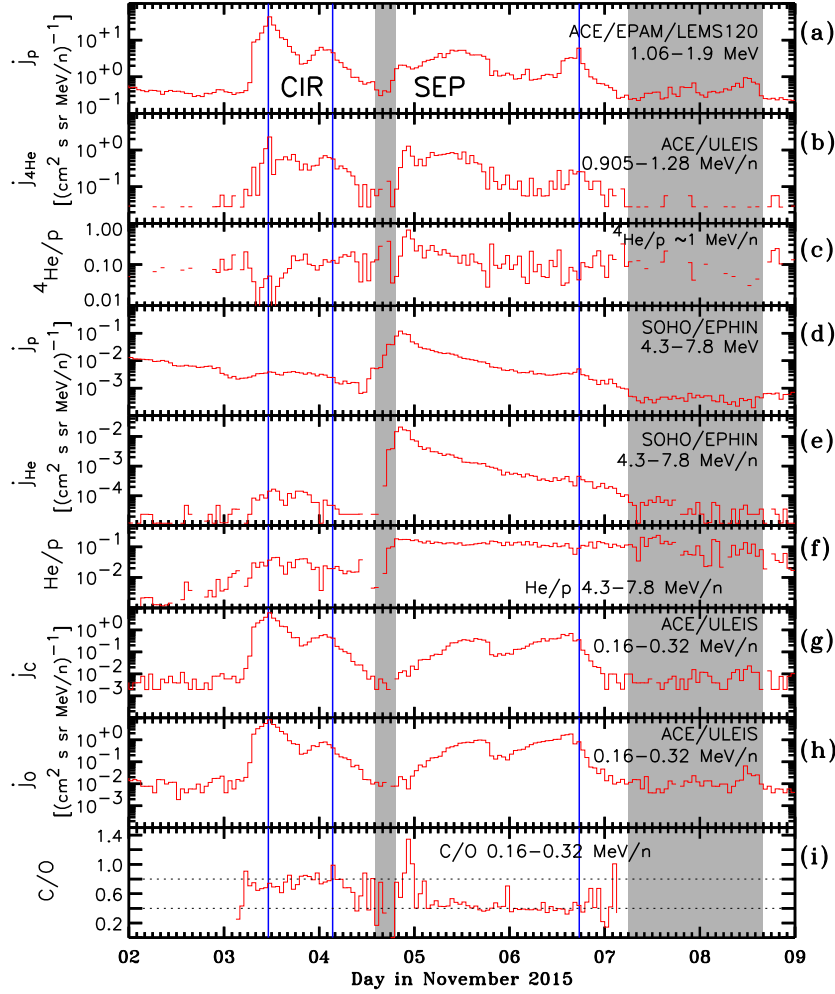


Figure 21. Intensities and abundance ratios of multiple energetic ions observed by ACE/EPAM, ACE/ULEIS and SOHO/EPHIN between November 2 and November 9, 2015: **a)** 1.06 – 1.9 MeV proton intensity, **b)** 0.905 – 1.28 MeV/n helium intensity, **c)** helium to proton abundance ratio at 1 MeV/n, **d)** 4.3 – 7.8 MeV proton intensity, **e)** 4.3 – 7.8 MeV/n helium intensity, **f)** 4.3 – 7.8 helium to proton ratio, **g)** 0.16 – 0.32 MeV/n carbon intensity, **h)** 0.16 – 0.32 MeV/n oxygen intensity, and **i)** 0.16 – 0.32 MeV/n carbon to oxygen ratio. Increases associated with CIRs and SEPs are labeled, as are ICME periods (shaded regions) and shocks (blue vertical lines).

of bidirectional distributions with an increase of sunward propagating electrons) signals that the spacecraft was inside an ICME. These electrons may have been reflected by the converging magnetic-field lines at the opposite ICME leg or by a reflecting magnetic barrier located significantly beyond 1 AU. In summary, the activity on 4 November 2015 was accompanied by an electron event (Event 1) that occurred in the sheath region between an ICME shock and its driver, and

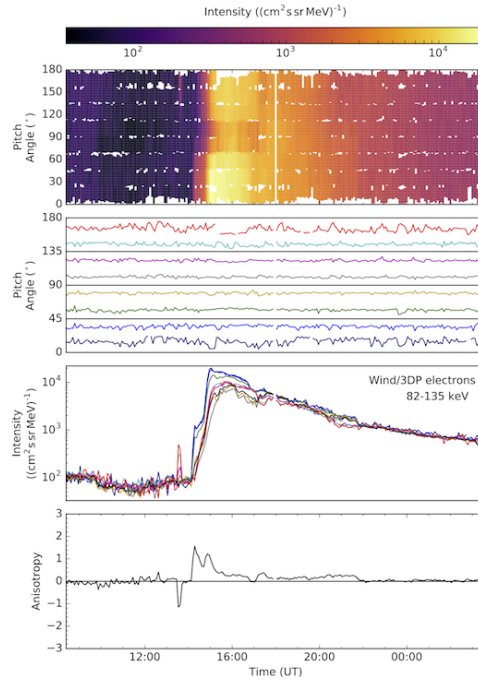


Figure 22. Energetic electron observations by *Wind*/3DP. From top to bottom: Pitch-angle distributions with color-coded intensity, pitch-angle corresponding to each pitch-angle bin, electron intensities observed in each bin, and the first-order anisotropy index. (The peaks near 13:30 – 13:45 UT in the bottom two panels are likely solar-flare light contamination and should be ignored.)

by an SEP event with enhanced proton and electron intensities (Event 3) that occurred within the magnetic obstacle of the ICME.

We modeled the early phase of the 82 – 135 KeV electron event observed by *Wind*/3DP using simulations of the interplanetary transport of solar energetic particles, followed by the optimization of the injection and transport parameters. The transport model (Agueda *et al.*, 2008) solves the focused transport equation (see Ruffolo, 1995, for the full equation), which is essentially one-dimensional along a magnetic field line. It assumes the electron solar source at $2 R_{\odot}$ and an Archimedean spiral magnetic-flux tube connecting the Sun and the spacecraft defined by the solar wind speed measured *in-situ*. (This approximation is not unreasonable for standard particle transport from the Sun but ignores the electrons observed moving Sunwards and this period’s ICME environment.) Interplanetary pitch-angle scattering is parametrized assuming a pitch-angle diffusion coefficient that resembles the predictions of the “standard model” (Jokipii, 1966; Jaekel and Schlickeiser, 1992): the mean free path characterizes the degree of pitch-angle scattering. Following previous works (*e.g.* Kallenrode, Wibberenz, and Huckle, 1992), we take the electron radial mean free path, λ_r , to be spatially constant. We used the SEPInversion software available in SEPServer (<http://server.sepserver.eu>) to infer the release time history and the value of the electron radial mean free

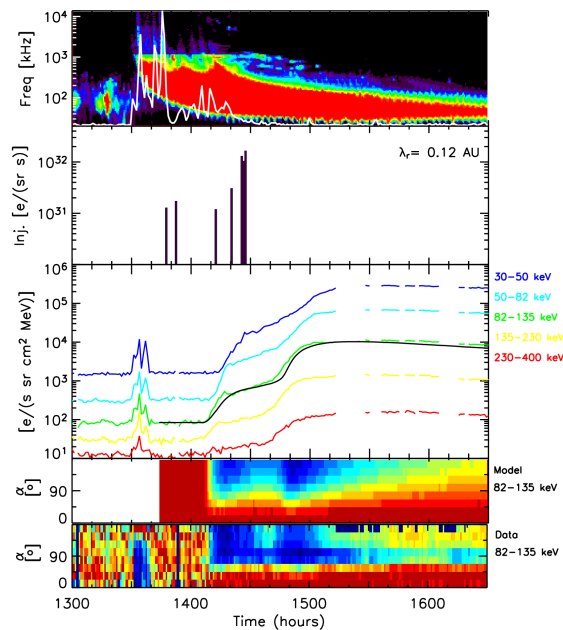


Figure 23. *From top to bottom:* Radio spectra observed by *Wind*/WAVES (colour-coded by intensity, with red large and black background) and 13 MHz microwave emission (white curve, relative intensity) on 4 November 2015 (for comparison purposes with the particle data, the emissions were shifted by -500 s); 82 – 135 KeV electron source profile deduced at $2 R_{\odot}$; omni-directional intensities observed by *Wind*/3DP in the energy range 30 – 400 KeV, with the black curve showing the best fit to the 82 – 135 KeV data for $\lambda_r = 0.12$ AU; the two bottom panels show the modeled and observed 82 – 135 KeV electron pitch-angle distributions normalized to the maximum value (1 = red to 0 = blue).

path. *SEPinversion* uses an inversion approach to fit the observations and it allows an estimation of the timing and intensity of the release without any *a priori* assumption on the profile.

Figure 23 shows the electromagnetic and particle data together with the best possible fit inferred using *SEPinversion*. The best fit (second panel) is obtained assuming $\lambda_r = 0.12$ AU and multiple electron injections that occur in two primary groups; this is sometimes loosely called a two-episode release time profile, but notice that the best-fit model contains at least six electron injections, not two. The finding of two primary groups of releases is qualitatively consistent with the two-episode injection scenario signalled by the anisotropy index (Figure 22, bottom panel).

Figure 23 shows that the model results cannot quantitatively explain the injection timing, as the two groups of inferred injections start ≈ 10 – 20 minutes after the beginning of the radio emission. The exact timing of the electron releases with respect to the electromagnetic emissions depends in part on the length of the interplanetary path, with a longer path allowing the injections to move earlier in time and so agree better with the radio events. The analysis in Figure 23 assumes a nominal Parker spiral, whereas the field line length may be different. For instance, since the electrons were detected within an ICME, the field lines

may be longer because of twisting (Kahler, Haggerty, and Richardson, 2011, but see). Alternatively, the field line that reaches Earth on 4 November in Figure 18 is predicted to have a length of 1.2 AU, while the nominal spiral is 1.1 AU long. This would allow the electrons to be released $\approx 0.1/1.1 \times 25 = 2.5$ minutes earlier, corresponding to moving the releases in Figure 23 to the left by 2.5 minutes. Since the impulsive coronal radio emissions start $\approx 10 - 20$ minutes earlier than the first set of predicted electron releases, the increased field line lengths in Figure 18 are insufficient to explain the timing difference. Instead, an enhanced field-line length in the range 1.5 – 1.9 AU is required, a clear quantitative problem.

The two groups of releases inferred from the modeling at first glance appear to agree with the two main groups of radio emissions apparent in the 13 MHz emissions in Figure 23 (top panel, white curve) near $\approx 13:30 - 13:45$ and $13:50 - 14:20$ UT. However, Figure 15 clearly shows multiple individual Type IIIs below ≈ 1 MHz throughout the approximate period $13:30 - 14:30$ UT, although above about ≈ 4 MHz separation into two groups appears reasonable. Evidence thus exists for Type III electron beams that are radio-quiet above ≈ 4 MHz but radio-loud below ≈ 1 MHz, as modelled by Li and Cairns (2012, 2013). The radio emissions and the Langmuir waves and energetic electrons observed at 1 AU show release of electrons into interplanetary space that are connected to L1. The concept of Type III cannibalism (Li, Robinson, and Cairns, 2002) is a plausible way to explain qualitatively why the multiple distinct decametric Type IIIs observed correspond to only two distinct signatures in the electron pitch-angle data.

7.3. SEP Proton Event Modeling

As summarised in Section 2, there are many challenges involved in modelling specific SEP events quantitatively, with many formalisms, models, and approximations involved. The approach adopted here is to present a modelling challenge to the community for the events of 4 November 2015 and to present one unusual analysis (that includes drift effects but assumes a constant, energy-independent, mean free path along Parker spiral fields) whose surprisingly good results are intended to stimulate the community into a concerted effort.

Analysis and interpretation of energetic protons observed from the 4 November 2015 events were hampered by the rotation of SOHO, which resulted in the ERNE instrument pointing perpendicular to the mean Parker spiral direction. Thus, applicable flux anisotropy profiles are not available and an analogue to the inversion method used for electrons in Section 7.2 is not possible. Similarly, although *Wind*/3DP observed flux anisotropies below 11 MeV (not shown here), the observations were inadequate for producing reliable inversion results.

An alternative to applying an inversion method to data to obtain the particle transport parameters and mean free paths (usually assuming transport confined to a single field line) is to allow for drifts and cross-field motion and to assume values for the prevalent mean free paths. This approach can also place constraints on the magnetic connectivity between the SEP source and observing location. Accordingly, we performed a number of simulations of SEP (proton) transport for the 4 November 2015 events using the full-orbit propagation model

of Marsh *et al.* (2013), capable of accounting for drifts and deceleration effects. The input database was constructed using the approximation of a constant, energy-independent, proton mean free path of 0.3 AU.

The results of the simulations were fed into the SEP forecasting tool described by Marsh *et al.* (2015), assuming a solar wind speed of 700 km s^{-1} (see Figure 19) and the associated Parker-spiral magnetic field connectivity for an assumed unipolar outward-pointing field at the coronal base. (See the comments in Section 7.2 about the actual magnetic environment.) The tool generates synthetic time profiles for protons at 1 AU by assuming injection at a flare-related shock, with a width of 48 degrees centered at the flare location, and with the injection constrained by the observed magnitude of the soft X-ray flare and a published correlation between soft X-ray flare magnitude and peak SEP intensity (Dierckx *et al.*, 2015).

For the foregoing parameters, the simulation tool predicts only barely observable (proton) SEP levels for Events 1 and 2, as shown by the fluxes predicted before 15:00 UT in Figure 24, not inconsistent with the observations in Figure 20. The situation is different for Event 3, for which Figure 24 displays both the flux of 12.6 – 53.5 MeV protons observed at SOHO/ERNE and the flux of 10 – 60 MeV protons predicted by the simulation tool. (For this event an additional static background flux of $10^{-3} \text{ protons cm}^{-2} \text{ s}^{-1} \text{ sr}^{-1}$ was added to the tool's predictions to produce the displayed results.)

Figure 24 suggests that the Marsh *et al.* (2015) model predicts the existence, timing, and qualitative size (within one to two orders of magnitude) of Event 3's SEPs quite well. Additional support for the model working surprisingly well (despite ignoring the ICME environment and non-Parker field lines) is that running the simulation for $v_{sw} = 500 \text{ km s}^{-1}$, corresponding to more common solar-wind speeds, and associated Parker magnetic connectivity leads to the prediction of SEPs for Events 1 and 2 but no SEPs for Event 3. These aspects are both inconsistent with the observations in Figures 20 and 24.

More detailed comparisons of the predicted and observed proton fluxes in Figure 24 illustrate the important roles of magnetic connectivity. First, while the observed and predicted onsets are very similar (near 15:30 UT), the peaks are not. The decline after the observed peak at approximately 20:00 UT coincides with a return to outwards magnetic polarity (near 19:45 UT on 4 November in Figure 19 that is not included in the model). Second, the time profiles for Event 3 and the low observed and predicted proton fluxes for Events 1 and 2 shown in Figure 24 are strong evidence that the proton SEP event observed at 1 AU on 4 November is due to Event 3, located near the central meridian and that the effective solar-wind speed $v_{sw} \approx 700 \text{ km s}^{-1}$. Third, for Event 3, connectivity to Earth (SOHO) is sub-optimal, with the early phase of the event not resulting in any flux. Rather, connected field lines sweep over the observer at 1 AU after the flare has occurred, consistent with a near-isotropic proton population impacting the SOHO/ERNE detector (which was pointing perpendicular to the mean magnetic-field direction). Differences in onset time between simulations and observations may be due to variations in the exact shape of the interplanetary magnetic field, the proton mean free path, or the spatial extent of the acceleration region at the Sun. Fourth, we further deduce

that the decay of the fluxes may be due to the non-trivial magnetic connectivity, and the transition between magnetic-field polarities. This is consistent with recent studies in SEP propagation, which confirm that magnetic polarity reversal boundaries are efficient at preventing particles from crossing them (Battarbee, Dalla, and Marsh, 2017).

Further work might follow several approaches: First, to repeat the foregoing analysis for multiple mean free paths so as to find the optimum value, requiring extensive computational resources not available to our collaboration. Second, to include the non-Parker-like fields in Figure 18 into the foregoing orbit calculations (Zhang, Qin, and Rassoul, 2009; Marsh *et al.*, 2013) and to compare the theoretical results, thereby directly assessing the importance of non-Parker fields for this event. Third, to perform the more standard analyses that include diffusive shock acceleration, scattering, magnetic focusing, and cross-field transport in one dimension (Li *et al.*, 2009; Verkhoglyadova *et al.*, 2010; Vainio *et al.*, 2014; Dröge *et al.*, 2014; He and Wan, 2015; Hu *et al.*, 2017) and in two dimensions (Hu *et al.*, 2017), thereby allowing assessment of the different physics included and of multi-dimensional effects. Finally, the CMEs, shocks, and background medium should be modelled as accurately as possible using multi-dimensional MHD simulations (Kozarev *et al.*, 2013; Schmidt, Cairns, and Hillan, 2013; Schmidt *et al.*, 2016; Hu *et al.*, 2017) and coupled with particle acceleration formalisms (Verkhoglyadova *et al.*, 2010; Kozarev *et al.*, 2013; Hu *et al.*, 2017) to predict the SEP properties, with comparisons elucidating the roles of the shock evolution, 3D background plasma, non-Parker magnetic fields, and the physical processes considered.

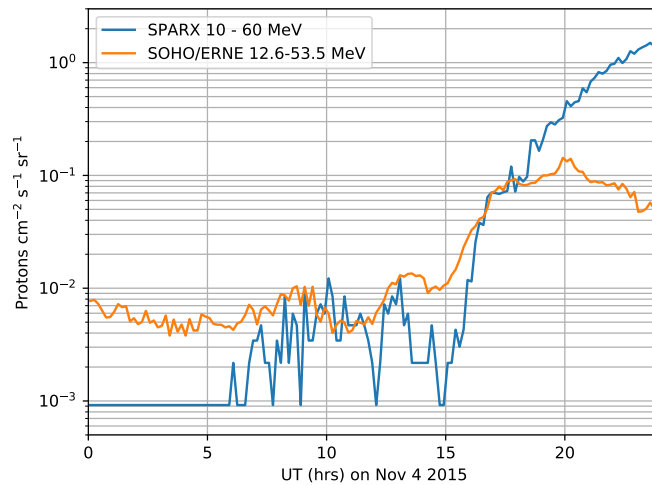


Figure 24. Combined integral ERNE HED proton observations on 4 November for 12.6 – 53.5 MeV (*orange*) are compared with the temporal profile predicted for 10 – 60 MeV protons by the SPARX forecasting software (*blue*), assuming a mean solar wind speed of 700 km s^{-1} . At the time of this event, SOHO was rotated 180 degrees, so ERNE was pointing perpendicular to the mean magnetic field.

8. Space Weather: Event Timing and Characteristics

Event 3 occurred near the centre of the solar disk and was associated with a broad CME and extended dimming regions most clearly seen in AIA images in the 193Å and 211Å channels (Figure 9). Its angular width was estimated to be 226° by CACTus (Robbrecht and Berghmans, 2004). Such a CME is generally thought to be Earth-directed. Accordingly, NOAA/SWPC made predictions of the arrival of the CME-driven shock wave at the Earth. This was part of their routine solar wind prediction using the WSA-ENLIL model (see www.swpc.noaa.gov/products/wsa-enlil-solar-wind-prediction). A pressure pulse representing the CME is inserted at ENLIL’s inner boundary at 21.5 R_{\odot} . The required CME parameters consist of the time at which the CME passes the heliocentric distance of 21.5 R_{\odot} , the direction (latitude and longitude), width (half angle), and radial velocity of the CME. After Event 3, three runs were made with different CME parameters as we can see in the NGDC archive (www.ngdc.noaa.gov/enlil). The parameters used in these three ENLIL runs are summarized in Table 2.

The prediction that was closest to the actual shock arrival (6 November 2015, 17:34 UT) was made at 20:00 UT on 4 November (≈ 6.5 hours after the flare onset). This is shown in Figure 25. The predicted arrival was 06:00 UT on 7 November. The other two runs predicted later arrivals (15:00 UT on 7 November and 03:00 UT the next day), indicating the present capability for predicting the CME shock arrival time is $\approx \pm 12$ hours (Vršnak *et al.*, 2014). Note that the CME parameters were obtained using only Earth-based observations, since STEREO A and B had not resumed operations after their solar-opposition passes earlier in 2015. Therefore, there were large uncertainties in obtaining the parameters of the cone model. Another source that affects the CME propagation in heliospheric simulations is how well the ambient solar wind is characterized (Vršnak *et al.*, 2013). Including the CMEs associated with Events 1 and 2, there were several CMEs of different sizes and speeds within a few days before Event 3, so it is possible that the actual heliosphere encountered by Event 3’s CME was significantly different than modelled in the ENLIL simulations.

A different method to estimate interplanetary travel times of ICMEs was proposed by Salas-Matamoros and Klein (2015) and Salas-Matamoros, Klein, and Trottet (2017). These authors used the fluence of the soft X-ray or microwave (8.8 GHz) burst associated with the CME to estimate the propagation speed of the CME front. This speed estimate is fed into the empirical propagation model of Gopalswamy *et al.* (2001) to predict the arrival time at 1 AU of the ICME’s magnetic cloud, rather than the shock. The SXR burst of 4 November 2015 in the 0.1 – 0.8 nm band rose to a maximum of about $3 \cdot 10^{-5} \text{ W m}^{-2}$ within about 22 minutes, producing a fluence of about $2.6 \cdot 10^{-2} \text{ J m}^{-2}$. The CME speed inferred from the empirical relationship given by Equation 2 of Salas-Matamoros and Klein (2015) is 950 km s^{-1} . The estimated arrival time at 1 AU is then 05:20 UT on Nov 07.

ACE/SWEPAM solar wind data (Figure 19) show that a time interval where the proton temperature is less than half the expected value for a standard solar wind stream (Elliott *et al.*, 2005) starts at 6 UT (between 5:53 and 6:21 UT) on

7 November. At about the same time the solar wind speed starts a systematic decrease which lasts over several hours. These indications of the arrival of the ICME at ACE are close to the time predicted using the SXR burst fluence, within ≈ 1 hour.

Microwave observations from the Sagamore Hill station of the *RSTN* show an impulsive burst ($\approx 13:37$ – $13:47$ UT) that rises to a peak flux of 782 sfu at 8.8 GHz and has a weak longer-lasting tail (not shown). The weak tail is probably thermal bremsstrahlung. The impulsive burst has a fluence of $1.5 \cdot 10^{-17} \text{ J m}^{-2} \text{ Hz}^{-1}$. Equation 1 and the coefficients for 9 GHz in Table 2 of Salas-Matamoros, Klein, and Trottet (2017) translate this into a CME speed of 460 km s^{-1} , which leads to an arrival prediction of 16:35 UT on 8 November. This is clearly much later than observed: the microwave method leads to a considerable underestimation of the CME speed in the corona. Comparing the predictions using the SXR burst fluence *versus* the microwaves for Event 3 suggests that the SXR method is considerably more accurate in this particular case. This agreement is exciting and suggests that the methods of Salas-Matamoros, Klein, and Trottet (2017) need to be tested in detail for additional events.

Once at Earth the CME related to Event 3 produced a set of space weather phenomena. Indeed, Figure 19 shows multiple southwards excursions of B_z in the sheath region between the shock and the tangential discontinuity in front of the CME material, together with a smooth rotation of θ_{RTN} and B_z changing from southwards to northwards. A standard geomagnetic substorm occurred with a sudden storm commencement and a significant intensification of the ring current and auroral zone activity. Specifically, the minimum D_{st} was ≈ -100 nT and the AE and Kp indices were enhanced from the shock arrival until about 2000 UT on 7 November (maximum values ≈ 1500 nT and 6, respectively) when B_z returned to being northwards.

A major space-weather effect of Event 3 was that the Swedish aviation radar systems were severely impacted by an extremely strong radio burst at GHz frequencies (Opgenoorth *et al.*, 2016). The effect was also seen in other European countries. The extreme intensity of the radio burst was only in a limited frequency range. A detailed study by Marqué *et al.* (2018) shows that the perturbations coincide in time with two intense peaks of the radio bursts near the operational frequencies of the secondary air traffic control radar. This makes the radio burst the prime candidate to explain the Swedish air traffic incident. Such radio bursts may be outside the usual space-weather forecasts. At least, the impact of such events appears to be both temporally and spatially limited.

9. Discussion and Conclusions

The solar events of 4 November 2015 present an ideal case for a multi-instrument and multi-event study with similar, closely spaced in time, events that are different in detail. They also provide a very good opportunity to address some of the current discrepancies in the observations and theory of solar activity. All three events had associated M-class X-ray flares, EUV waves, CMEs, and CME-driven shocks. The first two events occurred near the western limb above AR

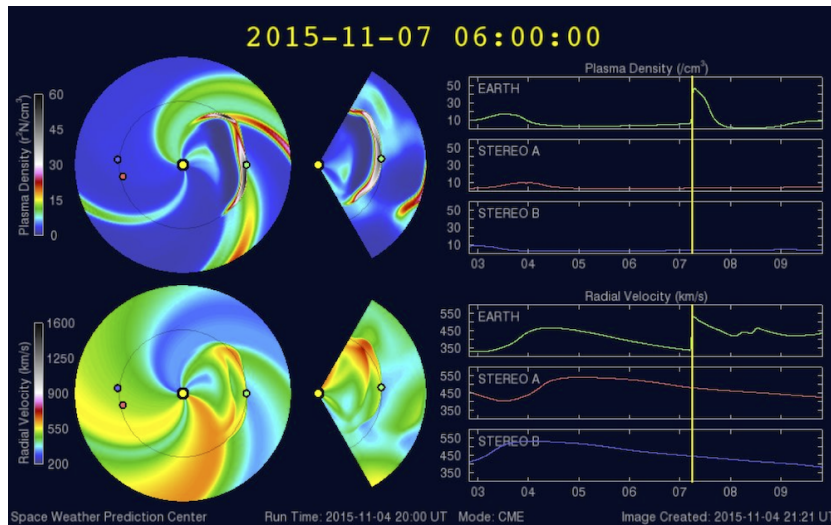


Figure 25. Snapshots of spatial maps in (*left*) the ecliptic plane and (*middle*) the meridional plane through the Sun-Earth line, as well as (*right*) temporal variations at Earth’s location for the (*upper row*) plasma density and (*lower row*) plasma speed. According to this run, the predicted shock-arrival time was 06:00 UT on 7 November 2015.

Table 2. CME parameters used for ENLIL runs by NOAA/SWPC

ID ^a	t_{CME} ^b	Lat.	Long.	Half Angle	Vel. ^c	Time (predicted)
1	4 Nov 19:00	11	7	53°	828	7 Nov 06:00
2	4 Nov 20:29	-12	35	38°	584	8 Nov 03:00
3	4 Nov 19:28	2	12	48°	762	7 Nov 15:00

a. The ID corresponds to the time at which ENLIL was run: 1. 20:00 on 4 November, 2. 00:00 on 5 November and 3. 02:00 on 5 November.

b. The time at which the CME is at $21.5 R_{\odot}$.

c. Radial velocity in km s^{-1}

12445, which showed very rapid emergence (in just three to four days). They were homologous with similar characteristics but also had differences. Their EUV waves were mostly directed southward from the active region, with the brightest parts being low above the solar disk. Any shocks likely occurred close to the source (consistent with the weak Moreton wave observed), and along the dominant direction of propagation southward from the source region. The first outburst had a strong microwave flare, observed by the Nobeyama radioheliograph and polarimeters; its X-ray and microwave properties point to a very strongly localised and low source, consistent with the high starting frequency for a Type II burst. Event 2, however, had only a weak microwave burst but came from the same active region.

Events 1–3 each produced a Type II burst, none of them identical or simple. Each can be interpreted in terms of multiple-lanes and/or split-bands and both fundamental and harmonic emission, often with very different intensities. Event 3

can be interpreted in terms of at least three Type II bursts or one Type II burst with at least six multiple lanes and split-bands. The Type II (and III) bursts observed should be excellent tests of theory, as well as the current understanding of their association with flare, CME, and SEP phenomena.

Events 1 and 2 had unusually high-frequency Type II bursts, either high-frequency Type III bursts cutoff below ≈ 100 MHz (Event 1) or no metric Type III bursts (Event 2), and minimal interplanetary Type III emission. These characteristics, especially the relative lack of interplanetary Type III activity, suggest that the associated shocks and flare sites were, despite both producing compact HXR sources seen by RHESSI, unable to produce accelerated particles that could either i) escape effectively into the high corona and interplanetary space, or ii) effectively produce radio emission in these regions, or iii) both. The absence of Type III emission at meter and longer wavelengths has long been recognized as a typical property of strong flares in the western solar hemisphere that are not accompanied by SEP events (Klein, Trottet, and Klassen, 2010; Klein *et al.*, 2011). We emphasize nevertheless that electron beams can be present but radio-quiet in some frequency domains and radio-loud in others (Li and Cairns, 2012, 2013), as observed here for Event 3.

It is important to outline the connection between the dynamics of filament eruptions, EUV waves, CMEs, and Type II radio bursts for the homologous Events 1 and 2. Given the observational evidence, we provide one possible scenario. With the onset of the flares, relatively bright, impulsive EUV fronts were launched both on-disk and off-limb, reaching quite high speeds ($\gtrsim 900$ km s⁻¹) early in the eruptions. The primarily south to southwest propagation direction for both was likely due to a “funnel” of weaker magnetic fields in that direction. This funnel may have focused the energy of the eruptions, allowing them to reach the high EUV intensity and speeds observed. The Type II bursts for both Events 1 and 2 began shortly after the onset of these bright, southward-directed EUV waves, indicating that the waves may have steepened into shocks quite early on and produced the radio emission. The Type II burst of Event 1 was much wider in frequency coverage than that of Event 2, indicating simultaneous emission from a range of coronal densities/heights, which agrees broadly with the EUV observations of the southern EUV front. The Type II burst continued for about ten minutes after the EUV front had left the AIA field of view. The EUV front of Event 2 had a smaller instantaneous height extent, was dimmer, and the associated Type II burst was narrower in frequency range and duration. We thus find strong temporal correlation, as well as qualitative correspondence between both the characteristics of the EUV and radio emission, and the scale of the two Types of emission, by comparing the two events.

Shortly after the onset of these seemingly impulsive EUV fronts, they were followed by much slower but persistent partial filament eruptions – initially in the southwest direction, eventually turning to the West. These drove the coronal waves in the west- and north-west directions, which eventually appeared as the bright CME fronts in coronagraphs. However, the slow filament eruptions only added to the fronts’ energy for a short period of time, their peak speeds approaching the weak CME speeds, and decreasing afterwards. This may explain why the CMEs were weak, slow, and short-lived – especially the CME of Event

2, which only had a failed filament eruption drive it. The slowness of the CMEs, despite the existence of fast wave-like disturbances in the low corona (the EUV waves), may be why the CMEs did not produce any Type II bursts in the high corona, as the Type II emission ended before the CMEs appeared in the LASCO C2 field of view. In the case of Event 2, the CME appeared in C2 a full half-hour after the Type II burst had ended.

Another important point is that the filament eruptions and EUV waves for Events 1 and 2 propagated primarily in the south to southwest directions, whereas the corresponding CMEs moved primarily west to northwest. This may have been due to the southwest-propagating off-limb portions of the EUV waves being decelerated by the overdense coronal plasma of the streamer, in which the flare site was embedded. At the same time, the radial portion of the compressive front kept propagating out through less dense material, additionally being driven by the partial filament eruptions. All of the above considerations lead us to conclude that the weak shock waves in Events 1 and 2 occurred early in the events, in the low corona, and were likely co-spatial to the observed EUV wavefronts. No Type II emission was observed after the EUV waves subsided, the quickly dissipating CMEs being the only interplanetary signatures of the events.

The *in-situ* particle observations show a lack of high-energy protons for the first two events, while energetic electrons were observed only for Event 1. This is despite the nominally good magnetic connections for both the flare and CME sources (see Section 6 and 7, however). The CMEs from the first two events were directed mostly westwards near the Ecliptic from the west-limb active region, and exhibited a typical dome-like structure, even if the EUV waves were observed to propagate predominantly southward.

Event 3, in contrast to Events 1 and 2, was associated with lower frequency Type II emission, a very long-lasting Type IV burst between at least 10 GHz and a few tens of MHz, and with coronal and interplanetary Type III bursts throughout the period 13:40–14:30 UT. Most but not all of these Type IIIs continue from above 10 MHz to below 1 MHz, with many of those that are not continuous appearing to be radio-quiet in the approximate domain 4 – 30 MHz, but radio-loud at higher and lower frequencies. The first Type IIIs started during the HXR and microwave bursts and can be connected qualitatively by timing observations, the theoretical SEP transport model of Agueda *et al.* (2008), and significantly longer, non-Parker, field lines to the first set of SEP electrons observed by the *Wind*/3DP instrument. There are quantitative difficulties, however, with field line lengths of 1.5 – 1.9 AU needed but available models (Figure 18) only yielding $\approx 1.1 - 1.2$ AU. The timing and two-step nature of the SEP electron profile despite having relatively continuous Type IIIs below ≈ 4 MHz, at least some of which are not seen in the ORFÉES and DAM spectra below about 30 MHz, and more than two injections in the transport model's best-fit solution all require further work. Consideration of better magnetic field connectivity models, the ICME environment, cannibalisation of Type III electron streams (Li, Robinson, and Cairns, 2002), and some electron beams being radio-quiet in some frequency domains and radio-loud in others (Li and Cairns, 2012, 2013)

appear necessary. Event 1 should also be modelled using this approach and associated implications drawn.

Some of Event 3's Type III bursts appear to be restricted to frequencies below the frequencies of simultaneous Type II bursts. One interpretation of this is that the shock wave producing the Type II bursts is also an accelerator of the electrons that produce Type III bursts, a possible alternative to the usual scenario that Type III electron beams originate in magnetic reconnection regions. Alternatively, the Type III streams originate below the Type II shock but only become radio-loud after crossing the shock (Li and Cairns, 2012). Another alternative is that the "missing" Type III radiation is generated outside of the CME and shock plasma but is prevented from reaching the observers at 1 AU by propagation effects associated with the high-density regions behind the shock and CME.

The third event's CME was a half-halo in the southern hemisphere from the central disk active region. It showed much higher speeds in LASCO data than the first two. It drove an interplanetary shock; both the CME and shock reached Earth unexpectedly quickly (in \approx two days), were not robustly or adequately predicted by ENLIL, and caused a space weather event with a geomagnetic storm. Interestingly, the SXR peak fluence method of Salas-Matamoros, Klein, and Trotter (2017) predicted Event 3's arrival well and should be tested more.

While SEP electrons were observed for Event 1, SEP protons were not and no SEPs were observed for Event 2. The relative lack of significant SEPs for these western events, despite the nominally good magnetic connectivity, the relatively bright EUV waves, and the intense, high frequency Type II bursts, may be due to the strong deceleration and narrow extents of the CME-driven shocks and so their inability to produce significant particle energization in the low corona. This is supported by the observed EUV disturbances and CMEs being fast and slow, respectively. The absence of strong Type III bursts for these events is an indication that the flare-accelerated particles either remained confined in the low corona or else were present but radio-quiet. Event 1's SEP electrons provide direct evidence for the radio-quiet interpretation (Li and Cairns, 2012, 2013). In addition, clearly, if there were significant flare- or shock-accelerated SEP protons for Event 1 or any SEPs at all for Event 2 then they did not find their way to open field lines connected to L1. This might be due to propagation effects or to particle injection onto non-connected field lines. Our magnetic-mapping and proton-transport analyses provide good evidence that the magnetic connectivity was not nominal for Events 1 and 2. Additionally, the CME eruptions were not radial for these events, complicating the study of connection points between the shock, flare site, and 1 AU. More detailed modelling of these events is required to differentiate between these interpretations. Even now, however, the analyses cast significant doubt on the typical relevance of simple connection analyses.

Event 3 actually produced significant levels of both electron and proton SEPs near 1 AU, consistent with the observation of a rather fast and broad CME and with Type III bursts that argue for particle escape from the active region. The SEP event had very different electron and ion behaviors: a prompt, two-step profile for the electrons with rapid rises (near 14:10 and 14:40 UT, respectively) and obvious (by factors of 10 – 100) flux increases for 35 – 500 KeV electrons,

versus prompt (starting around 15:00 UT), slow rise (peak near 20:00 UT), and subtle (by $< 50\%$) flux increase for 10 – 140 MeV ions, with some evidence for 1 MeV ion increases and little below that energy. Focusing on the protons, since the electron SEPs and Type IIIs are discussed earlier, the proton acceleration and transport model of Marsh *et al.* (2015) leads to surprisingly reasonable agreement with the existence, onset time, single peak nature, and qualitative size of Event 3’s proton SEP event. It also predicts weak, near background, fluxes of 10 – 60 MeV SEP protons for Events 1 and 2 that cannot be ruled out yet observationally. The model does not include the ICME environment or non-Parker field lines but shows strong magnetic connectivity effects, since changing the solar wind speed (and associated Parker connectivity) to 500 km s^{-1} from the observed value $\approx 700 \text{ km s}^{-1}$ leads to the prediction of clearly observable SEPs for Events 1 and 2 but none for Event 3, inconsistent with the observations. Future modelling work must address these effects.

In summary, the three events that occurred on 4 November 2015 show both similarities and differences from standard events and each other, despite having very similar interplanetary conditions and only two flare sites and CME genesis regions. They are therefore targets for further in-depth observational studies, and for testing both existing and new theories and models, of flares, CMEs, the acceleration and transport of energetic particles, Type II, III, IV, microwave, and SA bursts, and related SEPs. Comparing the remote and *in-situ* observations of the three events, it remains possible that two traits of CME-related SEP-rich events are having i) sustained Type II emission to low enough frequencies and ii) a sustained high-speed shock, in order to ensure sufficient energization of the particles. It is also possible that once the SEPs have gained enough energy, they can scatter efficiently perpendicularly to the magnetic field and so perfect magnetic connectivity is not required for them to reach the 1 AU observer. However, the results of this article show that magnetic connectivity is often not nominal (*e.g.* well described by a Parker spiral) and that both flare and CME sources of SEPs exist and may co-exist. While many aspects of Event 3’s SEPs can be explained by the models presented, multiple aspects of the foregoing plasma, radio, X-ray, and energetic particle phenomena remain unexplained in detail at this time. More elaborate descriptions of the coronal shock dynamics and dynamic magnetic connectivity conditions are necessary for the study of both early-stage and later SEPs, particularly for widely separated observers. In addition, the results of this work reveal the complexity and interrelation of the chain of phenomena associated with solar eruptions. They demonstrate the need for strong integration of *in-situ* and remote magnetic, spectroscopic, particle, radio, and X-ray observations of active regions, flares, CMEs, radio and X-ray emissions, and SEPs with advanced theoretical models in order to gain deeper and more correct understanding of these phenomena.

Acknowledgments The authors thank ISSI Bern for their hospitality to and support of the International Team on “The Connection Between Coronal Shock Wave Dynamics and Early SEP Production”, from which the majority of this work resulted. A. Veronig acknowledges Austrian Science Fund (FWF) grant P27292-N20. D. Lario was supported by NASA grants NNX15AD03G and NNX16AF73G ■

and the NASA Program NNH17ZDA001N-LW. N. Nitta acknowledges support from NSF grant AGS-1259549. This work utilizes data obtained by the Global Oscillation Network Group (GONG) program, managed by the National Solar Observatory, which is operated by AURA, Inc. under a cooperative agreement with the National Science Foundation. It also uses data acquired by instruments operated by the Big Bear Solar Observatory, High Altitude Observatory, Learmonth Solar Observatory, Udaipur Solar Observatory, Instituto de Astrofísica de Canarias, and Cerro Tololo Interamerican Observatory. Data from the SOHO/ERNE instrument was provided by the Space Research Laboratory at the University of Turku, Finland. The authors thank all groups providing data.

References

- Afanasiev, A., Vainio, R.: 2013, Monte Carlo simulation model of energetic proton transport through self-generated Alfvén waves. *Astrophys. J. Suppl.* **207**, 29. DOI. ADS.
- Agueda, N., Vainio, R., Lario, D., Sanahuja, B.: 2008, Injection and interplanetary transport of near-relativistic electrons: Modeling the impulsive event on 2000 May 1. *Astrophys. J.* **675**, 1601. DOI. ADS.
- Agueda, N., Klein, K.-L., Vilmer, N., Rodríguez-Gasén, R., Malandraki, O.E., Papaioannou, A., Subirà, M., Sanahuja, B., Valtonen, E., Dröge, W., Nindos, A., Heber, B., Braune, S., Usoskin, I.G., Heynderickx, D., Talew, E., Vainio, R.: 2014, Release timescales of solar energetic particles in the low corona. *Astron. Astrophys.* **570**, A5. DOI. ADS.
- Axisa, F.: 1974, On the role of the magnetic configuration of flares for production of Type III solar radio bursts. *Solar Phys.* **35**, 207. DOI. ADS.
- Bain, H.M., Krucker, S., Glesener, L., Lin, R.P.: 2012, Radio imaging of shock-accelerated electrons associated with an erupting plasmoid on 2010 November 3. *Astrophys. J.* **750**, 44. DOI. ADS.
- Baker, D.N., Kanekal, S.G., Hoxie, V.C., Henderson, M.G., Li, X., et al: 2013, A long-lived relativistic electron storage ring embedded in Earth's outer Van Allen belt. *Science* **340**, 44. DOI. ADS.
- Bale, S.D., Reiner, M.J., Bougeret, J.-L., Kaiser, M.L., Krucker, S., Larson, D.E., Lin, R.P.: 1999, The source region of an interplanetary type II radio burst. *Geophys. Res. Lett.* **26**, 1573. DOI. ADS.
- Bastian, T.S., Benz, A.O., Gary, D.E.: 1998, Radio emission from solar flares. *Annu. Rev. Astron. Astrophys.* **36**, 131. DOI. ADS.
- Battarbee, M., Dalla, S., Marsh, M.S.: 2017, Solar energetic particle transport near a heliospheric current sheet. *Astrophys. J.* **836**, 138. DOI. ADS.
- Battarbee, M., Vainio, R., Laitinen, T., Hietala, H.: 2013, Injection of thermal and suprathermal seed particles into coronal shocks of varying obliquity. *Astron. Astrophys.* **558**, A110. DOI. ADS.
- Bougeret, J.-L., Zarka, P., Caroubalos, C., Karlický, M., Leblanc, Y., Maroulis, D., Hillaris, A., Moussas, X., Alissandrakis, C.E., Dumas, G., Perche, C.: 1998, A shock-associated (SA) radio event and related phenomena observed from the base of the solar corona to 1 AU. *Geophys. Res. Lett.* **25**, 2513. DOI. ADS.
- Brueckner, G.E., Howard, R.A., Koomen, M.J., Korendyke, C.M., Michels, D.J., Moses, J.D., Socker, D.G., Dere, K.P., Lamy, P.L., Llebaria, A., Bout, M.V., Schwenn, R., Simnett, G.M., Bedford, D.K., Eyles, C.J.: 1995, The Large Angle Spectroscopic Coronagraph (LASCO). *Solar Phys.* **162**, 357. DOI. ADS.
- Cairns, I.H.: 1986, The source of free energy for Type II solar radio bursts. *Proc. of the Astron. Soc. Aust.* **6**, 444. ADS.
- Cairns, I.H.: 2011, In: Miralles, M.P., Sánchez Almeida, J. (eds.) *Coherent radio emissions associated with solar system shocks*, 267. ADS.
- Cairns, I.H., Schmidt, J.M.: 2015, Testing a theory for Type II radio bursts from the Sun to near 0.5 AU. *J. Phys. CS* **642**(1), 012004. DOI. ADS.

- Cairns, I.H., Knock, S.A., Robinson, P.A., Kuncic, Z.: 2003, Type II solar radio bursts: Theory and space weather implications. *Space Sci. Rev.* **107**, 27. DOI. ADS.
- Cane, H.V., Erickson, W.C.: 2005, Solar Type II radio bursts and IP Type II events. *Astrophys. J.* **623**, 1180. DOI. ADS.
- Cane, H.V., Stone, R.G.: 1984, Type II solar radio bursts, interplanetary shocks, and energetic particle events. *Astrophys. J.* **282**, 339. DOI. ADS.
- Cane, H.V., Erickson, W.C., Prestage, N.P.: 2002, Solar flares, Type III radio bursts, coronal mass ejections and energetic particles. *J. Geophys. Res.* **107**, 1315. DOI. ADS.
- Cane, H.V., McGuire, R.E., von Rosenvinge, T.T.: 1986, Two classes of solar energetic particle events associated with impulsive and long-duration soft X-ray flares. *Astrophys. J.* **301**, 448. DOI. ADS.
- Cane, H.V., Stone, R.G., Fainberg, J., Steinberg, J.L., Hoang, S., Stewart, R.T.: 1981, Radio evidence for shock acceleration of electrons in the solar corona. *Geophys. Res. Lett.* **8**, 1285.
- Carley, E.P., Long, D.M., Byrne, J.P., Zucca, P., Bloomfield, D.S., McCauley, J., Gallagher, P.T.: 2013, Quasiperiodic acceleration of electrons by a plasmoid-driven shock in the solar atmosphere. *Nature Physics* **9**, 811. DOI. ADS.
- Caspi, A., Krucker, S., Lin, R.P.: 2014, Statistical properties of super-hot solar flares. *Astrophys. J.* **781**, 43. DOI. ADS.
- Cohen, C.M.S.: 2006, Observations of energetic storm particles: An overview. *Amer. Geophys. Un. Geophys. Mon. Ser.*, Washington DC **165**. ADS.
- Dauphin, C., Vilmer, N., Krucker, S.: 2006, Observations of a soft X-ray rising loop associated with a type II burst and a coronal mass ejection in the 03 November 2003 X-ray flare. *Astron. Astrophys.* **455**, 339. DOI. ADS.
- Decker, R.B., Vlahos, L.: 1986, Numerical studies of particle acceleration at turbulent, oblique shocks with an application to prompt ion acceleration during solar flares. *Astrophys. J.* **306**, 710. DOI. ADS.
- Desai, M., Giacalone, J.: 2016, Large gradual solar energetic particle events. *Liv. Rev. Solar Phys* **13**, 3. DOI. ADS.
- Dierckxens, M., Tziotziou, K., Dalla, S., Patsou, I., Marsh, M.S., Crosby, N.B., Malandraki, O., Tsiropoula, G.: 2015, Relationship between solar energetic particles and properties of flares and CMEs: Statistical analysis of solar cycle 23 events. *Solar Phys* **290**, 841. <http://link.springer.com/10.1007/s11207-014-0641-4>.
- Downs, C., Roussev, I.I., van der Holst, B., Lugaz, N., Sokolov, I.V.: 2012, Understanding SDO/AIA observations of the 2010 June 13 EUV wave event: Direct insight from a global thermodynamic MHD simulation. *Astrophys. J.* **750**, 134. DOI. ADS.
- Dresing, N., Gómez-Herrero, R., Klassen, A., Heber, B., Kartavykh, Y., Dröge, W.: 2012, The large longitudinal spread of solar energetic particles during the 17 January 2010 solar event. *Solar Phys* **281**, 281. DOI. ADS.
- Dresing, N., Gómez-Herrero, R., Heber, B., Klassen, A., Malandraki, O., Dröge, W., Kartavykh, Y.: 2014, Statistical survey of widely spread out solar electron events observed with STEREO and ACE with special attention to anisotropies. *Astron. Astrophys.* **567**, A27. DOI. ADS.
- Dröge, W., Kartavykh, Y.Y., Dresing, N., Heber, B., Klassen, A.: 2014, Wide longitudinal distribution of interplanetary electrons following the 7 February 2010 solar event: Observations and transport modeling. *J. Geophys. Res. (Space Phys)* **119**, 6074. DOI. ADS.
- Elliott, H.A., McComas, D.J., Schwadron, N.A., Gosling, J.T., Skoug, R.M., Gloeckler, G., Zurbuchen, T.H.: 2005, An improved expected temperature formula for identifying interplanetary coronal mass ejections. *J. Geophys. Res.* **110**, A04103.
- Elliott, H.A., Henney, C.J., McComas, D.J., Smith, C.W., Vasquez, B.J.: 2012, Temporal and radial variation of the solar wind temperature-speed relationship. *J. Geophys. Res. (Space Phys)* **117**, A09102. DOI. ADS.
- Fletcher, L., Dennis, B.R., Hudson, H.S., Krucker, S., Phillips, K., Veronig, A., Battaglia, M., Bone, L., Caspi, A., Chen, Q., Gallagher, P., Grigis, P.T., Ji, H., Liu, W., Milligan, R.O., Temmer, M.: 2011, An observational overview of solar flares. *Space Sci. Rev.* **159**, 19. DOI. ADS.
- Fox, N.J., Velli, M.C., Bale, S.D., Decker, R., Driesman, A., Howard, R.A., Kasper, J.C., Kinnison, J., Kusterer, M., Lario, D., Lockwood, M.K., McComas, D.J., Raouafi, N.E., Szabo, A.: 2016, The Solar Probe Plus mission: Humanity's first visit to our star. *Space Sci. Rev.* **204**, 7. DOI. ADS.

- Gold, R.E., Krimigis, S.M., Hawkins, I. S. E., Haggerty, D.K., Lohr, D.A., Fiore, E., Armstrong, T.P., Holland, G., Lanzerotti, L.J.: 1998, Electron, proton, and alpha monitor on the Advanced Composition Explorer spacecraft. *Space Sci. Rev.* **86**, 541. DOI. ADS.
- Gómez-Herrero, R., Dresing, N., Klassen, A., Heber, B., Lario, D., Agueda, N., Malandraki, O.E., Blanco, J.J., Rodríguez-Pacheco, J., Banjac, S.: 2015, Circumsolar energetic particle distribution on 2011 November 3. *Astrophys. J.* **799**, 55. DOI. ADS.
- Gopalswamy, N., Lara, A., Yashiro, S., Kaiser, M.L., Howard, R.A.: 2001, Predicting the 1-AU arrival times of coronal mass ejections. *J. Geophys. Res.* **106**, 29207.
- Gopalswamy, N., Xie, H., Mäkelä, P., Yashiro, S., Akiyama, S., Uddin, W., Srivastava, A.K., Joshi, N.C., Chandra, R., Manoharan, P.K., Mahalakshmi, K., Dwivedi, V.C., Jain, R., Awasthi, A.K., Nitta, N.V., Aschwanden, M.J., Choudhary, D.P.: 2013, Height of shock formation in the solar corona inferred from observations of Type II radio bursts and coronal mass ejections. *Advances in Space Research* **51**, 1981. DOI. ADS.
- Haggerty, D.K., Roelof, E.C.: 2002, Impulsive near-relativistic solar electron events: Delayed injection with respect to solar electromagnetic emission. *Astrophys. J.* **579**, 841. DOI. ADS.
- Haggerty, D.K., Roelof, E.C., Simnett, G.M.: 2003, Escaping near-relativistic electron beams from the solar corona. *Advances in Space Research* **32**, 2673. DOI. ADS.
- He, H.-Q., Wan, W.: 2015, Numerical study of the longitudinally asymmetric distribution of solar energetic particles in the heliosphere. *Astrophys. J. Suppl.* **218**(2), 17. DOI. ADS.
- Holljoki, S., Pomoell, J., Vainio, R., Palmroth, M., Koskinen, H.E.J.: 2013, Interpreting solar EUV wave observations from different viewing angles using an MHD model. *Solar Phys.* **286**, 493. DOI. ADS.
- Holman, G.D., Pesses, M.E.: 1983, Solar Type II radio emission and the shock drift acceleration of electrons. *Astrophys. J.* **267**, 837. DOI. ADS.
- Holman, G.D., Aschwanden, M.J., Aurass, H., Battaglia, M., Grigis, P.C., Kontar, E.P., Liu, W., Saint-Hilaire, P., Zharkova, V.V.: 2011, Implications of X-ray observations for electron acceleration and propagation in solar flares. *Space Sci. Rev.* **159**, 107. DOI. ADS.
- Howard, T.A., Pizzo, V.J.: 2016, Challenging some contemporary views of coronal mass ejections. I. The case for blast waves. *J. Geophys. Res.* **824**, 92. DOI. ADS.
- Hu, J., Li, G., Ao, X., Zank, G.P., Verkhoglyadova, O.: 2017, Modeling particle acceleration and transport at a 2-D CME-driven shock. *J. Geophys. Res. (Space Phys)* **122**(11), 10,938. DOI. ADS.
- Hurford, G.J., Schmahl, E.J., Schwartz, R.A., Conway, A.J., Aschwanden, M.J., Csillaghy, A., Dennis, B.R., Johns-Krull, C., Krucker, S., Lin, R.P., McTiernan, J., Metcalf, T.R., Sato, J., Smith, D.M.: 2002, The RHESSI imaging concept. *Solar Phys.* **210**, 61. DOI. ADS.
- Jaekel, U., Schlickeiser, R.: 1992, Quasilinear theory of cosmic ray pitch-angle diffusion for generalized turbulence models. *Ann. Geophys.* **10**, 541. ADS.
- Jokipii, J.R.: 1966, Cosmic-ray propagation. I. Charged particles in a random magnetic field. *Astrophys. J.* **146**, 480. ADS.
- Jones, F.C., Ellison, D.C.: 1991, The plasma physics of shock acceleration. *Space Sci. Rev.* **58**, 259. DOI. ADS.
- Kahler, S.W., Haggerty, D.K., Richardson, I.G.: 2011, Magnetic Field-line Lengths in Interplanetary Coronal Mass Ejections Inferred from Energetic Electron Events. *Astrophys. J.* **736**(2), 106. DOI. ADS.
- Kallenrode, M.-B., Cliver, E.W., Wibberenz, G.: 1992, Composition and azimuthal spread of solar energetic particles from impulsive and gradual flares. *Astrophys. J.* **391**, 370. DOI. ADS.
- Kallenrode, M.-B., Wibberenz, G., Hücke, S.: 1992, Propagation conditions of relativistic electrons in the inner heliosphere. *Astrophys. J.* **394**, 351. DOI. ADS.
- Kennel, C.F., Coroniti, F.V., Scarf, F.L., Livesey, W.A., Russell, C.T., Smith, E.J., Wenzel, K.P., Scholer, M.: 1986, A test of Lee's quasi-linear theory of ion acceleration by interplanetary traveling shocks. *J. Geophys. Res.* **91**, 11917. DOI. ADS.
- Klassen, A., Aurass, H., Klein, K.-L., Hofmann, A., Mann, G.: 1999, Radio evidence on shock wave formation in the solar corona. *Astron. Astrophys.* **343**, 287. ADS.
- Klassen, A., Dresing, N., Gómez-Herrero, R., Heber, B., Müller-Mellin, R.: 2016, Unexpected spatial intensity distributions and onset timing of solar electron events observed by closely spaced STEREO spacecraft. *Astron. Astrophys.* **593**, A31. DOI. ADS.
- Klecker, B., Möbius, E., Popecki, M.A.: 2006, Solar energetic particle charge states: An overview. *Space Sci. Rev.* **124**, 289. DOI. ADS.
- Klecker, B., Kunow, H., Cane, H.V., Dalla, S., Heber, B., Kecskemety, K., Klein, K.-L., Kota, J., Kucharek, H., Lario, D., Lee, M.A., Popecki, M.A., Posner, A., Rodríguez-Pacheco, J.,

- Sanderson, T., Simnett, G.M., Roelof, E.C.: 2006, Energetic particle observations. *Space Sci. Rev.* **123**, 217. DOI. ADS.
- Klein, K.-L., Trotter, G., Klassen, A.: 2010, Energetic particle acceleration and propagation in strong CME-less flares. *Solar Phys.* **263**, 185. DOI. ADS.
- Klein, K.-L., Khan, J.I., Vilmer, N., Delouis, J.-M., Aurass, H.: 1999, X-ray and radio evidence on the origin of a coronal shock wave. *Astron. Astrophys.* **346**, L53. ADS.
- Klein, K.-L., Trotter, G., Samwel, S., Malandraki, O.: 2011, Particle acceleration and propagation in strong flares without major solar energetic particle events. *Solar Phys.* **269**, 309. DOI. ADS.
- Knock, S.A., Cairns, I.H., Robinson, P.A., Kuncic, Z.: 2001, Theory of Type II radio emission from the foreshock of an interplanetary shock. *Journal of Geophysical Research (Space Physics)* **106**, 25041. DOI. ADS.
- Knock, S.A., Cairns, I.H., Robinson, P.A., Kuncic, Z.: 2003, Theoretically predicted properties of Type II radio emission from an interplanetary foreshock. *Journal of Geophysical Research (Space Physics)* **108**, 1126. DOI. ADS.
- Kong, X., Chen, Y., Guo, F., Feng, S., Wang, B., Du, G., Li, G.: 2015, The possible role of coronal streamers as magnetically closed structures in shock-induced energetic electrons and metric Type II radio bursts. *Astrophys. J.* **798**, 81. DOI. ADS.
- Kozarev, K.A., Korreck, K.E., Lobzin, V.V., Weber, M.A., Schwadron, N.A.: 2011, Off-limb solar coronal wavefronts from SDO/AIA extreme-ultraviolet observations - implications for particle production. *Astrophys. J. Lett.* **733**, L25. DOI. ADS.
- Kozarev, K.A., Evans, R.M., Schwadron, N.A., Dayeh, M.A., Opher, M., Korreck, K.E., van der Holst, B.: 2013, Global numerical modeling of energetic proton acceleration in a coronal mass ejection traveling through the solar corona. *Astrophys. J.* **778**, 43. DOI. ADS.
- Kozarev, K.A., Raymond, J.C., Lobzin, V.V., Hammer, M.: 2015, Properties of a coronal shock wave as a driver of early SEP acceleration. *Astrophys. J.* **799**, 167. DOI. ADS.
- Krucker, S., Larson, D.E., Lin, R.P., Thompson, B.J.: 1999, On the origin of impulsive electron events observed at 1 AU. *Astrophys. J.* **519**, 864. DOI. ADS.
- Lario, D., Aran, A., Gómez-Herrero, R., Dresing, N., Heber, B., Ho, G.C., Decker, R.B., Roelof, E.C.: 2013, Longitudinal and radial dependence of solar energetic particle peak intensities: STEREO, ACE, SOHO, GOES, and MESSENGER observations. *Astrophys. J.* **767**, 41. DOI. ADS.
- Lario, D., Raouafi, N.E., Kwon, R.-Y., Zhang, J., Gómez-Herrero, R., Dresing, N., Riley, P.: 2014, The solar energetic particle event on 2013 April 11: An investigation of its solar origin and longitudinal spread. *Astrophys. J.* **797**, 8. DOI. ADS.
- Lario, D., Kwon, R.-Y., Riley, P., Raouafi, N.E.: 2017a, On the link between the release of solar energetic particles measured at widespread heliolongitudes and the properties of the associated coronal shocks. *Astrophys. J.* **847**, 103. DOI. ADS.
- Lario, D., Kwon, R.-Y., Richardson, I.G., Raouafi, N.E., Thompson, B.J., von Rosenvinge, T.T., Mays, M.L., Mäkelä, P.A., Xie, H., Bain, H.M., Zhang, M., Zhao, L., Cane, H.V., Papaioannou, A., Thakur, N., Riley, P.: 2017b, The solar energetic particle event of 2010 August 14: Connectivity with the solar source Inferred from multiple spacecraft observations and Modeling. *Astrophys. J.* **838**, 51. DOI. ADS.
- Lee, M.A.: 1983, Coupled hydromagnetic wave excitation and ion acceleration at interplanetary traveling shocks. *J. Geophys. Res.* **88**, 6109. DOI. ADS.
- Lee, M.A.: 2005, Coupled hydromagnetic wave excitation and ion acceleration at an evolving coronal/Interplanetary shock. *Astrophys. J. Suppl.* **158**, 38. DOI. ADS.
- Li, B., Cairns, I.H.: 2012, Type III radio bursts perturbed by weak coronal shocks. *Astrophys. J.* **753**, 124. DOI. ADS.
- Li, B., Cairns, I.H.: 2013, Type III radio bursts in coronal plasmas with kappa particle distributions. *Astrophys. J. Lett.* **763**, L34. DOI. ADS.
- Li, B., Cairns, I.H., Robinson, P.A.: 2008, Simulations of coronal Type III solar radio bursts: 1. Simulation model. *J. Geophys Res (Space Phys)* **113**, A06104. DOI. ADS.
- Li, B., Robinson, P.A., Cairns, I.H.: 2002, Multiple electron beam propagation and Langmuir wave generation in plasmas. *Phys Plasmas* **9**, 2976. DOI. ADS.
- Li, B., Cairns, I.H., Gosling, J.T., Steward, G., Francis, M., Neudegg, D., Schulte in den Bäumen, H., Player, P.R., Milne, A.R.: 2016, Mapping magnetic field lines between the Sun and Earth. *J. Geophys Res (Space Phys)* **121**, 925. DOI. ADS.
- Li, G., Zank, G.P., Rice, W.K.M.: 2005, Acceleration and transport of heavy ions at coronal mass ejection-driven shocks. *Journal of Geophysical Research (Space Physics)* **110**(A6), A06104. DOI. ADS.

- Li, G., Zank, G.P., Verkhoglyadova, O., Mewaldt, R.A., Cohen, C.M.S., Mason, G.M., Desai, M.I.: 2009, Shock geometry and spectral breaks in large SEP events. *Astrophys. J.* **702**(2), 998. DOI. ADS.
- Lin, R.P.: 1985, Energetic solar electrons in the interplanetary medium. *Solar Phys.* **100**, 537. DOI. ADS.
- Lin, R.P., Schwartz, R.A., Pelling, R.M., Hurley, K.C.: 1981, A new component of hard X-rays in solar flares. *Astrophys. J. Lett.* **251**, L109. DOI. ADS.
- Lin, R.P., Dennis, B.R., Hurford, G.J., Smith, D.M., Zehnder, A., Harvey, P.R., Curtis, D.W., Pankow, D., Turin, P., Bester, M., Csillaghy, A., Lewis, M., Madden, N., van Beek, H.F., Appleby, M., Raudorf, T., McTiernan, J., Ramaty, R., Schmahl, E., Schwartz, R., Krucker, S., Abiad, R., Quinn, T., Berg, P., Hashii, M., Sterling, R., Jackson, R., Pratt, R., Campbell, R.D., Malone, D., Landis, D., Barrington-Leigh, C.P., Slassi-Sennou, S., Cork, C., Clark, D., Amato, D., Orwig, L., Boyle, R., Banks, I.S., Shirey, K., Tolbert, A.K., Zarro, D., Snow, F., Thomsen, K., Henneck, R., McHedlishvili, A., Ming, P., Fivian, M., Jordan, J., Wanner, R., Crubb, J., Preble, J., Matranga, M., Benz, A., Hudson, H., Canfield, R.C., Holman, G.D., Crannell, C., Kosugi, T., Emslie, A.G., Vilmer, N., Brown, J.C., Johns-Krull, C., Aschwanden, M., Metcalf, T., Conway, A.: 2002, The Reuven Ramaty High-Energy Solar Spectroscopic Imager (RHESSI). *Solar Phys* **210**, 3. DOI. ADS.
- Luhmann, J.G., Mays, M.L., Odstrcil, D., Li, Y., Bain, H., Lee, C.O., Galvin, A.B., Mewaldt, R.A., Cohen, C.M.S., Leske, R.A., Larson, D., Futaana, Y.: 2017, Modeling solar energetic particle events using ENLIL heliosphere simulations. *Space Weather* **15**, 934. DOI. ADS.
- Luhn, A., Klecker, B., Hovestadt, D., Gloeckler, G., Ipavich, F.M., Scholer, M., Fan, C.Y., Fisk, L.A.: 1984, Ionic charge states of N, Ne, Mg, Si and S in solar energetic particle events. *Adv Space Res* **4**, 161. DOI. ADS.
- Luhn, A., Klecker, B., Hovestadt, D., Moebius, E.: 1987, The mean ionic charge of silicon in He-3-rich solar flares. *Astrophys. J.* **317**, 951. DOI. ADS.
- Ma, S., Raymond, J.C., Golub, L., Lin, J., Chen, H., Grigis, P., Testa, P., Long, D.: 2011, Observations and interpretation of a low coronal shock wave observed in the EUV by the SDO/AIA. *Astrophys. J.* **738**, 160. DOI. ADS.
- Marqué, C., Klein, K.-L., Monstein, C., Opgenoorth, H., Pulkkinen, A., Buchert, S., Krucker, S., Van Hoof, R., Thulesen, P.: 2018, Solar radio emission as a disturbance of aeronautical radionavigation. *J Space Weather Space Clim.* **8**, A42.
- Marsh, M.S., Dalla, S., Kelly, J., Laitinen, T.: 2013, Drift-induced perpendicular transport of solar energetic particles. *Astrophys. J.* **774**(1), 4. DOI. <http://adsabs.harvard.edu/abs/2013ApJ...774....4M>.
- Marsh, M.S., Dalla, S., Dierckx, M., Laitinen, T., Crosby, N.B.: 2015, SPARX: a modelling system for solar energetic particle radiation space weather forecasting. *Space Weather* **13**, 386. DOI.
- Mason, G.M., Sanderson, T.R.: 1999, CIR associated energetic particles in the inner and middle heliosphere. *Space Sci. Rev.* **89**, 77. DOI. ADS.
- Matthaeus, W.H., Qin, G., Bieber, J.W., Zank, G.P.: 2003, Nonlinear collisionless perpendicular diffusion of charged particles. *Astrophys. J. Lett.* **590**(1), L53. DOI. ADS.
- McCauley, P.I., Su, Y.N., Schanche, N., Evans, K.E., Su, C., McKillop, S., Reeves, K.K.: 2015, Prominence and filament eruptions observed by the Solar Dynamics Observatory: Statistical properties, kinematics, and online catalog. *Solar Phys* **290**, 1703. DOI. ADS.
- McComas, D.J., Bame, S.J., Barker, P., Feldman, W.C., Phillips, J.L., Riley, P., Griffee, J.W.: 1998, Solar Wind Electron Proton Alpha Monitor (SWEPAM) for the Advanced Composition Explorer. *Space Sci. Rev.* **86**, 563. DOI. ADS.
- Miteva, R., Klein, K.-L., Kienreich, I., Temmer, M., Veronig, A., Malandraki, O.E.: 2014a, Solar energetic particles and associated EIT disturbances in solar cycle 23. *Solar Phys.* **289**, 2601. DOI. ADS.
- Miteva, R., Klein, K.-L., Kienreich, I., Temmer, M., Veronig, A., Malandraki, O.E.: 2014b, Solar energetic particles and associated EIT disturbances in solar cycle 23. *Solar Phys.* **289**, 2601. DOI. ADS.
- Moreton, G.E.: 1960, H α observations of flare-initiated disturbances with velocities \sim 1000 km/sec. *Astron. J.* **65**, 494. DOI. ADS.
- Müller, D., Marsden, R.G., St. Cyr, O.C., Gilbert, H.R.: 2013, Solar Orbiter . Exploring the Sun-heliosphere connection. *Solar Phys.* **285**, 25. DOI. ADS.
- Müller-Mellin, R., Kunow, H., Fleißner, V., Pehlke, E., Rode, E., Röschmann, N., Scharmberg, C., Sierks, H., Ruzsnyak, P., McKenna-Lawlor, S., Elendt, I., Sequeiros, J., Meziat, D., Sanchez, S., Medina, J., Del Peral, L., Witte, M., Marsden, R., Henrion, J.: 1995, COSTEP

- Comprehensive Suprathermal and Energetic Particle Analyser. *Solar Phys.* **162**, 483. DOI. ADS.
- Nelson, G.J., Melrose, D.B.: 1985, In: McLean, D.J., Labrum, N.R. (eds.) *Type II bursts*, 333. ADS.
- Nelson, G.J., Robinson, R.D.: 1975, Multi-frequency heliograph observations of Type II bursts. *Proc Astron Soc Aust* **2**, 370. ADS.
- Ng, C.K., Reames, D.V., Tylka, A.J.: 2003, Modeling shock-accelerated solar energetic particles coupled to interplanetary Alfvén waves. *Astrophys. J.* **591**(1), 461. DOI. ADS.
- Nitta, N.V., Schrijver, C.J., Title, A.M., Liu, W.: 2013, Large-scale coronal propagating fronts in solar eruptions as observed by the Atmospheric Imaging Assembly on board the Solar Dynamics Observatory – an ensemble study. *J. Geophys. Res.* **776**, 58. DOI. ADS.
- Nitta, N.V., Liu, W., Gopalswamy, N., Yashiro, S.: 2014, The relation between large-scale coronal propagating fronts and Type II radio bursts. *Solar Phys.* **289**, 4589. DOI. ADS.
- Oppenorth, H., Pulkkinen, A., Buchert, S., Monstein, C., Klein, K.L., Marqué, C., Krucker, S.: 2016, Solar activity during the space weather incident of Nov 4., 2015 - Complex data and lessons learned. In: ???, *EGU Gen Ass Conf Abs* **18**, EPSC2016. ADS.
- Pacheco, D., Agueda, N., Gómez-Herrero, R., Aran, A.: 2017, Interplanetary transport of solar near-relativistic electrons on 2014 August 1 over a narrow range of heliolongitudes. *J Space Weather Space Clim.* **7**(27), A30. DOI. ADS.
- Parker, E.N.: 1958, Dynamics of the interplanetary gas and magnetic fields. *Astrophys. J.* **128**, 664. DOI. ADS.
- Patsourakos, S., Vourlidas, A.: 2012, On the nature and genesis of EUV Waves: A synthesis of observations from SOHO, STEREO, SDO, and Hinode (invited review). *Solar Phys.* **281**, 187. DOI. ADS.
- Patsourakos, S., Vourlidas, A., Stenborg, G.: 2010, The genesis of an impulsive coronal mass ejection observed at ultra-high cadence by AIA on SDO. *Astrophys. J. Lett.* **724**, L188. DOI. ADS.
- Pomoell, J., Vainio, R., Kissmann, R.: 2008, MHD modeling of coronal large-amplitude waves related to CME lift-off. *Solar Phys.* **253**, 249. DOI. ADS.
- Pötzi, W., Veronig, A.M., Riegler, G., Amerstorfer, U., Pock, T., Temmer, M., Polanec, W., Baumgartner, D.J.: 2015, Real-time flare detection in ground-based H α imaging at Kanzelhöhe Observatory. *Solar Phys.* **290**, 951. DOI. ADS.
- Reames, D.V.: 1988, Bimodal abundances in the energetic particles of solar and interplanetary origin. *Astrophys. J. Lett.* **330**, L71. DOI. ADS.
- Reames, D.V.: 1999, Particle acceleration at the Sun and in the heliosphere. *Space Sci. Rev.* **90**, 413. DOI. ADS.
- Reames, D.V., Stone, R.G.: 1986, The identification of solar He-3-rich events and the study of particle acceleration at the sun. *Astrophys. J.* **308**, 902. DOI. ADS.
- Reid, H.A.S., Ratcliffe, H.: 2014, A review of solar Type III radio bursts. *Res Astron Astrophys* **14**, 773. DOI. ADS.
- Reiner, M.J., Kaiser, M.L.: 1999, Complex Type III-like radio emissions observed from 1 to 14 MHz. *Geophys. Res. Lett.* **26**, 397. DOI. ADS.
- Reiner, M.J., Kaiser, M.L., Fainberg, J., Stone, R.G.: 1998, A new method for studying remote Type II radio emissions from coronal mass ejection-driven shocks. *J. Geophys. Res.* **103**, 29651. DOI. ADS.
- Robbrecht, E., Berghmans, D.: 2004, Automated recognition of coronal mass ejections (CMEs) in near-real-time data. *Astron. Astrophys.* **425**, 1097. DOI. ADS.
- Rouillard, A.P., Sheeley, N.R., Tylka, A., Vourlidas, A., Ng, C.K., Rakowski, C., Cohen, C.M.S., Mewaldt, R.A., Mason, G.M., Reames, D., Savani, N.P., StCyr, O.C., Szabo, A.: 2012, The longitudinal properties of a solar energetic particle event investigated using modern solar imaging. *J. Geophys. Res.* **752**, 44. DOI. ADS.
- Ruffolo, D.: 1995, Effect of adiabatic deceleration on the focused transport of solar cosmic rays. *Astrophys. J.* **442**, 861. DOI. ADS.
- Salas-Matamoros, C., Klein, K.-L.: 2015, On the statistical relationship between CME speed and soft X-ray flux and fluence of the associated flare. *Solar Phys.* **290**, 1337. DOI. ADS.
- Salas-Matamoros, C., Klein, K.-L., Trottet, G.: 2017, Microwave radio emission as a proxy of CME speed in ICME arrival predictions at 1 AU. *J. Space Weather Space Clim.* **7**, A2.
- Scherrer, P.H., Schou, J., Bush, R.I., Kosovichev, A.G., Bogart, R.S., Hoeksema, J.T., Liu, Y., Duvall, T.L., Zhao, J., Title, A.M., Schrijver, C.J., Tarbell, T.D., Tomczyk, S.: 2012, The Helioseismic and Magnetic Imager (HMI) Investigation for the Solar Dynamics Observatory (SDO). *Solar Phys.* **275**, 207. DOI. ADS.

- Schmidt, J.M., Cairns, I.H.: 2012, Type II radio bursts: 2. Application of the new analytic formalism. *J Geophys Res (Space Phys)* **117**, A11104. DOI. ADS.
- Schmidt, J.M., Cairns, I.H.: 2016a, Demonstration of a viable quantitative theory for interplanetary Type II radio bursts. In: *American Institute of Physics Conference Series, American Institute of Physics Conference Series* **1720**, 040014. DOI. ADS.
- Schmidt, J.M., Cairns, I.H.: 2016b, Quantitative prediction of Type II solar radio emission from the Sun to 1 AU. *Geophys Res Lett* **43**, 50. DOI. ADS.
- Schmidt, J.M., Cairns, I.H., Hillan, D.S.: 2013, Prediction of Type II solar radio bursts by three-dimensional MHD coronal mass ejection and kinetic radio emission simulations. *Astrophys. J. Lett.* **773**, L30. DOI. ADS.
- Schmidt, J.M., Cairns, I.H., Lobzin, V.V.: 2014, The solar Type II radio bursts of 7 March 2012: Detailed simulation analyses. *J Geophys Res (Space Phys)* **119**, 6042. DOI. ADS.
- Schmidt, J.M., Cairns, I.H., Xie, H., St. Cyr, O.C., Gopalswamy, N.: 2016, CME flux rope and shock identifications and locations: Comparison of white light data, Graduated Cylindrical Shell model, and MHD simulations. *J Geophys Res (Space Phys)* **121**, 1886. DOI. ADS.
- Schrijver, C.J., De Rosa, M.L.: 2003, Photospheric and heliospheric magnetic fields. *Solar Phys.* **212**, 165. DOI. ADS.
- Schulte in den Bäumen, H., Cairns, I.H., Robinson, P.A.: 2011, Modeling 1 AU solar wind observations to estimate azimuthal magnetic fields at the solar source surface. *Geophys. Res. Lett.* **38**, L24101. DOI. ADS.
- Schulte in den Bäumen, H., Cairns, I.H., Robinson, P.A.: 2012, Nonzero azimuthal magnetic fields at the solar source surface: Extraction, model, and implications. *J Geophys Res (Space Physics)* **117**(16), A10104. DOI. ADS.
- Shalchi, A., Li, G., Zank, G.P.: 2010, Analytic forms of the perpendicular cosmic ray diffusion coefficient for an arbitrary turbulence spectrum and applications on transport of Galactic protons and acceleration at interplanetary shocks. *Astrophys. Space Sci.* **325**(1), 99. DOI. ADS.
- Smith, C.W., L'Heureux, J., Ness, N.F., Acuña, M.H., Burlaga, L.F., Scheifele, J.: 1998, The ACE magnetic fields experiment. *Space Sci. Rev.* **86**, 613. DOI. ADS.
- Suzuki, S., Dulk, G.A.: 1985, In: McLean, D.J., Labrum, N.R. (eds.) *Bursts of Type III and Type V*, 289. ADS.
- Temmer, M., Vršnak, B., Veronig, A.M.: 2013, The wave-driver system of the off-disk coronal wave of 17 January 2010. *Solar Phys.* **287**, 441. DOI. ADS.
- Thompson, B.J., Plunkett, S.P., Gurman, J.B., Newmark, J.S., St Cyr, O.C., Michels, D.J.: 1998, Soho/eit observations of an earth-directed coronal mass ejection on may 12, 1997. *Geophys. Res. Lett.* **25**, 2465. DOI. ADS.
- Torsti, J., Valtonen, E., Lumme, M., Peltonen, P., Eronen, T., Louhola, M., Riihonen, E., Schultz, G., Teittinen, M., Ahola, K., Holmlund, C., Kelh , V., Lepp l , K., Ruuska, P., Str mmer, E.: 1995, Energetic Particle Experiment ERNE. *Solar Phys.* **162**, 505. DOI. ADS.
- Torsti, J., Kocharov, L.G., Teittinen, M., Thompson, B.J.: 1999, Injection of 10 MeV protons in association with a coronal Moreton wave. *Astrophys. J.* **510**, 460. DOI. ADS.
- Torsti, J., Kocharov, L., Laivola, J., Lehtinen, N., Kaiser, M.L., Reiner, M.J.: 2002, Solar particle event with exceptionally high ³He enhancement in the energy range up to 50 MeV nucleon⁻¹. *Astrophys. J. Lett.* **573**, L59. DOI. ADS.
- Uchida, Y.: 1968, Propagation of hydromagnetic disturbances in the solar corona and moreton's wave phenomenon. *Solar Phys.* **4**, 30. DOI. ADS.
- Vainio, R., P nni, A., Battarbee, M., Koskinen, H.E.J., Afanasiev, A., Laitinen, T.: 2014, A semi-analytical foreshock model for energetic storm particle events inside 1 AU. *J. Space Weather Space Clim.* **4**(27), A08. DOI. ADS.
- Verkhoglyadova, O.P., Li, G., Zank, G.P., Hu, Q., Cohen, C.M.S., Mewaldt, R.A., Mason, G.M., Haggerty, D.K., von Rosenvinge, T.T., Looper, M.D.: 2010, Understanding large SEP events with the PATH code: Modeling of the 13 December 2006 SEP event. *Journal of Geophysical Research (Space Physics)* **115**(A12), A12103. DOI. ADS.
- Veronig, A.M., Muhr, N., Kienreich, I.W., Temmer, M., Vršnak, B.: 2010, First observations of a dome-shaped large-scale coronal extreme-ultraviolet wave. *Astrophys. J. Lett.* **716**, L57. DOI. ADS.
- Vourlidis, A., Wu, S.T., Wang, A.H., Subramanian, P., Howard, R.A.: 2003, Direct detection of a coronal mass ejection-associated shock in Large Angle and Spectrometric Coronagraph experiment white-light images. *J. Geophys. Res.* **598**, 1392. DOI. ADS.

- Vršnak, B., Warmuth, A., Temmer, M., Veronig, A., Magdalenic, J., Hillaris, A., Karlický, M.: 2006, Multi-wavelength study of coronal waves associated with the CME-flare event of 3 November 2003. *Astron. Astrophys.* **448**, 739. DOI. ADS.
- Vršnak, B., Žic, T., Vrbanec, D., Temmer, M., Rollett, T., Möstl, C., Veronig, A., Čalogović, J., Dumbović, M., Lulić, S., Moon, Y.-J., Shanmugaraju, A.: 2013, Propagation of interplanetary coronal mass ejections: The drag-based model. *Solar Phys.* **285**, 295. DOI. ADS.
- Vršnak, B., Temmer, M., Žic, T., Taktakishvili, A., Dumbović, M., Möstl, C., Veronig, A.M., Mays, M.L., Odstrčil, D.: 2014, Heliospheric propagation of coronal mass ejections: Comparison of numerical WSA-ENLIL+Cone model and analytical drag-based model. *Astrophys. J. Suppl.* **213**, 21. DOI. ADS.
- Warmuth, A.: 2007, Large-scale waves and shocks in the solar corona. In: Klein, K.-L., MacKinnon, A.L. (eds.) *The High Energy Solar Corona: Waves, Eruptions, Particles, Lecture Notes in Physics* **725**, Springer, Berlin; New York, 107. DOI. ADS.
- Warmuth, A., Mann, G.: 2005, A model of the Alfvén speed in the solar corona. *Astron. Astrophys.* **435**, 1123. DOI. ADS.
- Warmuth, A., Vršnak, B., Magdalenic, J., Hanslmeier, A., Otruba, W.: 2004, A multiwavelength study of solar flare waves. II. Perturbation characteristics and physical interpretation. *Astron. Astrophys.* **418**, 1117. DOI. ADS.
- Webb, D.F., Howard, T.A.: 2012, Coronal mass ejections: Observations. *Liv. Rev. Solar Phys* **9**(3). DOI. <http://www.livingreviews.org/lrsp-2012-3>.
- Zank, G.P., Rice, W.K.M., Wu, C.C.: 2000, Particle acceleration and coronal mass ejection driven shocks: A theoretical model. *J. Geophys. Res.* **105**(A11), 25079. DOI. ADS.
- Zhang, M., Qin, G., Rassoul, H.: 2009, Propagation of solar energetic particles in three-dimensional interplanetary magnetic fields. *Astrophys. J.* **692**(1), 109. DOI. ADS.
- Zimovets, I., Vilmer, N., Chian, A.C.-L., Sharykin, I., Struminsky, A.: 2012, Spatially resolved observations of a split-band coronal Type II radio burst. *Astron. Astrophys.* **547**, A6. DOI. ADS.
- Zucca, P., Pick, M., Démoulin, P., Kerdraon, A., Lecacheux, A., Gallagher, P.T.: 2014, Understanding coronal mass ejections and associated shocks in the solar corona by merging multi-wavelength observations. *J. Geophys. Res.* **795**, 68. DOI. ADS.